UNIVERISTY OF CALIFORNIA
RIVERSIDE

Measurements of the Casmir Pressure at Low Temperature

A Dissertation submitted in partial satisfaction
of the requirements for the degree of

Doctor of Philosophy

in

Physics

by

José-Rodrigo Castillo-Garza

March 2011

Dissertation Committee:
Professor Umar Mohideen, Chairperson
Professor Harry Tom
Professor Roya Zandi

The Dissertation of José-Rodrigo Castillo-Garza is approved:

_____

_____

_____

Committee Chairperson

University of California, Riverside

ACKNOWLEDGEMENTS

I would like to thank Professor Mohideen for giving me the opportunity to work in this important and exciting topic. I am also grateful for the advice and support of my committee members, Professor Tom and Professor Zandi.

My sincerest thanks to my labmates, Erick and Douglas. I would also like to thank Prof. Bayermann, for his help in low temperature physics and all the experimental support.

I express my deepest gratitude to my wonderful family. I thank my parents, who has always believed in me and encouraged me to do my best. I thank my wife's parents for all the support during these arduous years.

To my wife…thanks is not enough!

DEDICATION

To her and the one that came after her…

ABSTRACT OF THE DISSERTATION

Measurements of the Casmir Pressure at Low-Temperature

by

José-Rodrigo Castillo-Garza

Doctor of Philosophy, Graduate Program in Physics
University of California, Riverside, March 2011
Dr. Umar Mohideen, Chairperson

The role of material losses in the Casimir force and its incorporation into the Lifshitz theory of the Casimir force remains unresolved. This force results from the modification of the zero point photon spectra due to the presence of boundaries. The problem arises when the Casimir force is calculated at non-zero temperatures for real materials boundaries. This means that the contribution of the thermal photons must be added to that of the zero point photons while both contributions satisfying non-ideal boundary conditions. We address this problem by dynamically measuring the Casimir pressure between two parallel plates at T = 6.7 K, T = 77 K, and T = 300 K. At these temperatures, we have measured the Casmir pressure between gold coated substrates in the range 120 nm to 600 nm. To measure it we use a variable temperature atomic force microscope that we designed and built at UC-Riverside. Particularly at T = 6.7 K, the relative percent error of the experimental values is < 1 % in the range 150 nm to 230 nm. In addition, these results have less than 2% degree of agreement with the corresponding

theoretical values calculated using the generalized Drude-like model. This precision is sufficient to measure the thermal effects of the Casmir pressure predicted by the generalized Drude-like model. The outcome of these results will deepen our understanding of the mechanisms that virtual photons use to exchange energy with real materials. Moreover, they are bound to have a technological impact in the nanotechnology industry.

Table of Contents

List of Figures

1 Introduction

The Casimir force belongs to a group of forces that are induced by fluctuations. These forces have an entropic origin and are found throughout Nature [4]. They surface when certain characteristic parameter of the fluctuations is large enough to interact with distant macroscopic boundaries. When these boundaries confine the fluctuations, hence limiting the entropy in the confined space, the result is an attractive force between them. This force is a consequence of the system's drive to minimize such a space. These forces are mostly due to quantum vacuum fluctuations or thermal fluctuations.[4] Quantum vacuum fluctuations, for example, have an infinite range and give rise to the Casimir force. In contrast, thermal fluctuations have a range that depends on the parameters of the system and are responsible for forces of classical origin. Such are the cases of the Critical Casimir force [5] and the force decreasing the thickness of a superfluid Helium (^{4}He) film wetting a substrate [6]. Interestingly, the Critical Casimir force has been measured in two different systems: One of them consists of two surfaces that confine a binary liquid mixture close to its critical point [6]. The other is a ^{4}He film at the vicinity of the superfluid/normal transition, where, due to finite-size scaling, the Critical Casimir force thins the film [6]. In summary, a force will attract the boundaries that confine long-range fluctuations, either of classical or quantum origin. Additionally, the entropic nature of these forces does not allow them to be compensated, which is in contrast to electrostatic, magnetic, or gravitational forces, where corresponding opposite fields can result in a net force equal to zero.

The subject of this manuscript centers on the Casimir force between metallic

surfaces, which as mentioned previously, a force that is due to the quantum vacuum fluctuations. These fluctuations are essential for quantum field theories as they describe the states that exist in the absence of sources. For the case of Quantum Electrodynamics (QED), these states correspond to the virtual photons, and their energy is the zero-point energy of the electromagnetic (EM) fields. These photons are claimed to be responsible for the Lamb shift, anomalous magnetic moment of the electron, the Unruh effect, and the Casimir effect [7]. It has even been suggested that the zero-point energy of the EM fields contributes to the cosmological constant [8]. Nevertheless, the reality of these quantum vacuum fluctuations has been contested [9]. In part this is because they have not been experimentally observed but mainly because the effects mentioned above can be explained without reference to these fluctuations. Such is the case for the Casimir phenomena, which can be explained as a relativistic quantum effect between multiple EM induced dipoles [7]. This view is related to the Van der Waals forces, however, it will not be described in this manuscript because it has been shown to be equivalent to the quantum vacuum fluctuations approach [7]. Since the quantum vacuum fluctuations play such a central role in the simplest description of many phenomena, more exploration is needed.[10]

The Casimir force is one tool to explore the quantum vacuum and the properties of its zero-point fluctuations. In 1948, Hendrick Casimir showed that the attractive force between parallel plates is due to the quantum vacuum fluctuations [11], a pioneering result that lead to more inquires about the nature of these fluctuations. To obtain this result he calculated the zero-point energy inside and outside of a cavity formed by two

parallel plates. He used the ideal metal approximation, $\varepsilon(\omega) \rightarrow \infty$, for the plates and assumed they were at the same electrostatic potential. He then calculated the energy difference between these two regions. Surprisingly, the result is a finite value that is independent of any renormalization function. The expression he obtained for the force between the plates is the following:

$$F_0 = \left(\frac{\pi^2 \hbar c}{240}\right) \frac{1}{d^4} \cdot A \qquad 1.1$$

Here F_0 is denotes the Casimir force. The value d is the separation distance between the plates and A is the area of the plates. About a decade later, E. Lifshitz derived a macroscopic theory for the Casimir force with a more realistic view of the materials that confine the quantum vacuum fluctuations [12]. Moreover, this includes the effects that thermal photons have on the Casimir force. To be specific, using the fluctuation-dissipation theorem, he calculated the force assuming the plates to be dielectrics at a non-zero temperature. His result is currently used to obtain the accuracy of Casimir force experiments [13]. In this theoretical approach, the constituent material of the plates is characterized through their electric permittivity. Their explicit form is established when the theoretical model describing the material is selected. For example, using the Schwinger's prescription [14], Lifshitz's approach reproduces the expression in eq. 1 when $\varepsilon(\omega) \rightarrow \infty$ is taken before considering temperature effects. It is worth noting that a better theoretical description of the plates will provide a better understanding of the interactions between the vacuum fluctuations and real materials. Of utmost importance

however, is that the results obtained by Lifshitz and Casimir produced ways to investigate the quantum vacuum from the interaction of real macroscopic objects.

These results have had a technological impact and a growing interest in the micro and nano machines community [15]. Due to the continuous miniaturization of devices and the lack of control of the Casimir force, the semiconductor industry has had to engineer devices with actuators -most likely a spring- that compensates for this force [16]. This approach has been used in several current working devices but is not always reliable [16]. The actuators are prone to wear, loose elastic properties, and eventually deteriorate. The idea of replacing them is, in most cases, nearly impossible and not cost effective. Furthermore, continuous device miniaturization will increase the role of the Casimir force in these technologies [15]. For example, using Eq. 1.1, when d = 10 nm the Casimir pressure is 1 atm. This means that there will need to be a more sophisticated approach to dealing with this force. A possible way to achieve this is to better understand the quantum vacuum fluctuations when they are confined. This could possibly result in the ability to control the Casimir force, which will minimize the need for actuators that compensate this force. In addition, the control of the Casimir force could eventually lead to using it as the driving force behind future nano devices.

These conclusions have led researchers to setup experiments to study the quantum vacuum through the Casimir force. Since 1958, Sparnaay [17] and others [18-20] have carried out experiments, mostly between parallel plates, that attempted to measure this force. Unfortunately, the results of those experiments were only qualitative. Either they did not have enough force sensitivity or they had large systematic errors and were unable

to provide quantitative conclusions. Nevertheless, their results provided direction to the field and some measurement standards that are still followed today [13]. In contrast, recent experiments have used high-precision instruments to measure the Casimir force. They have used instruments such as the atomic force microscope (AFM) [21-23]and sensitive microelectromechanical devices (MEMS) [2, 24]. Their results have achieved a precision of around 1% with such a high accuracy that theoretical models can be put to the test. Another key factor is that the experiments performed with these instruments have extensive work on reducing systematic errors and surface preparation of the substrates. Such efforts have allowed them to fully investigate the behavior of the quantum vacuum fluctuations when they are confined.

The resurgence of interest in the Casimir force dates to a demonstration experiment by Lamoreaux in 1997 [25]. The instrument he used was a torsion balance that measured the Casimir force between a metal-coated lens and a plate with a similar coating. His results, while better than those obtained in previous experiments, were not sufficiently precise to increase the understanding of the quantum vacuum.[13, 26] This is not the case for later experiments by Mohideen et al. and the experiments that that followed [21-23, 27, 28]; their 1% precision is not only more than an order of magnitude better than the precision of Lamoreaux's experiment, but their accuracy is higher as well. This is because they used high-precision instruments and their data is compared to more specific models of the metal-coated plates. Their results, obtained with similar lens-plate setups, have uncovered several properties of the quantum vacuum through the Casimir force. For instance, they found a geometry dependence of the force, which accounts for

diffraction-like effects on the fluctuations and the non-additivity of the Casimir force [22]. Furthermore, many of these precise experiments have been geared towards the understanding of the interaction of the vacuum fluctuations with real materials. For example, since plates are intrinsically rough, they measured the roughness and corrected the measured force [28]. They also modified the electrical and optical properties of the plates to better understand the connection between the electric permittivity of the plates and the quantum vacuum fluctuations [23, 27]. This last decade has seen numerous precise Casimir force experiments that have enhanced our understanding of the quantum vacuum.

Although these experiments have covered much ground, there still remains considerable number of paradoxes [13, 29, 30]. One of them is the role played by the dissipation of the constituent material of the plates in the Casimir force. Dissipation, which accounts for the relaxation processes of the conduction electrons, is a part of the response of any material to EM fields. Particularly at non zero-temperatures, the influence that the dissipation has on the material's response has been a subject of recent theoretical controversy [10, 13, 31, 32]. For two plates in thermal equilibrium, the dispute arises because temperature accentuates distinct behaviors of the force for different models of the plates' electric permittivity. For example, when the plates are metallic, simple models of the permittivity, such as the Drude or the Plasma model, produce different numerical values of the Casimir force. In addition to this highly debated difference, Drude-type models do not reproduce the ideal metal value of the force [13]. Although this is not universally accepted [33-35], this is not the sole detractor of these types of models.

For sufficiently low temperatures and in combination with Lifshitz's approach, they produce large thermal corrections to the force and violate the third law of Thermodynamics [13]; this is in contrast to calculating the force using the electric permittivity described with Plasma-type models, which have no fundamental problems. Regardless, Drude-type models are promoted because they describe more accurately the response of the plates' material to EM fields, especially when compared to models such as the Plasma model -a more phenomenological approach. According to the competing factions in the Casimir field, models that are more accurate should be employed to compare with experimental measurements. However, within the Lifshitz's approach, the current more accurate models have troublesome consequences. Simpler models do not have these issues; hence, the paradox.

As mentioned above, it is predicted that temperature accentuates different behaviors of the Casimir force for different theoretical models of the plates; therefore, performing experiments in a region where temperature can influence the Casimir force is essential. This has not been the case, however, since all experiments have been performed at room temperature and at separations between the plates of less than 1 micron. With these parameters, most experimental efforts to measure the effects of material dissipation at non-zero temperatures on the Casimir force have not been convincing [25]. The main reason is that they have not had sufficient force resolution to detect the thermal effects of this force. High resolution is paramount because thermal effects have a minute influence on the Casimir force at room temperature, and at plates' separation of less than 6 micron. It is only recently that a thermal correction due to the Drude model has been excluded

experimentally [36]. The experiment that observed it was performed at room temperature, between two gold (Au) coated substrates, and at distances between the substrates of less that 1 micron. These observations claim to be able to discern between two of the competing theories that describe the plates. However, these results have been contested and it has been suggested by various researches that they are not definitive. They assert that the accuracy of these measurements is overestimated [37]. Other researchers advocate that these results are explained with a more rigorous theoretical formulation of the model of the constituent material of the plates [38]. It is nevertheless general consensus that more precise, higher resolution experiments are required to resolve this subject.

It is the purpose of this manuscript to present an experimental study of the Casimir force induced by quantum vacuum fluctuations. The objective of this study is two fold: To understand the role of material dissipation in the Casimir force at non-zero temperatures, and to precisely measure the Casimir pressure between two metal plates separated up to 1.5 micrometers. To achieve these objectives we have designed and constructed a high resolution atomic force microscope capable of precise measurements. This microscope functions in a high vacuum environment and at various temperatures: At room temperature, 77 K, and at 6.7 K. Its high resolution is reached with a dynamic technique that measures the gradient of the studied force. Pragmatism has shown experimenters in this field that this gradient should be measured between a sphere and a substrate, instead of between two flat plates. This microscope follows this approach. After certain mathematical manipulation, the outcome of these measurements can be related to

the Casimir pressure between two flat plates. While similar instruments [2, 24, 39] have already used dynamic techniques to study the Casimir force, none of them has used them in a low temperature environment. The advantage and particularity of using our microscope in this environment is that it has the potential to have greater resolution than its counterparts do at room temperature. Therefore, in principle, this microscope should have enough resolution to distinguish between the two competing theories regarding material dissipation. In conclusion, we expect its results to shed some light on the way the quantum vacuum fluctuations interact with the dissipative materials that confine them. In addition, they should allow technologists to have a clearer picture of the scenarios devices will encounter when size scales drop far below 1 micron.

This thesis contains seven chapters. The first one is the introduction. The second chapter describes a theoretical formulation of the Casmir force at zero temperature in the plate-plate configuration and in the sphere-plate configuration. The following chapter presents the same formalism from chapter two but for the Casmir force at non-zero temperatures. In this third chapter, we also review some material models that are relevant for the measurement of the force and present the controversial results that researchers have obtained. In the fourth chapter, we review previous techniques to measure the Casmir force and some of its most relevant accomplishments. Additionally, we present the technique used by the authors of this manuscript to measure the Casmir force and the reasons why it has the potential to increase the force resolution by several orders of magnitude. The fifth chapter describes the most relevant features of the experimental apparatus used by the authors to explore the Casmir effect and in the sixth chapter; the

results and the analysis of the measurements are presented. Chapter 7 concludes the thesis with a review of the accomplishments and future prospects of this experimental study.

2 Casimir force at zero Kelvin

In this chapter, there are two sections with different derivations of the Casimir force between parallel plates, both of them assuming that the temperature is zero. The first section treats the material boundaries as ideal metals, similar to the approach followed by H. Casimir. The resulting expression is used in the next subsection to briefly describe the Proximity Force Approximation, a necessary step to obtain an approximate value of the Casimir force between a sphere and a plate. The second section contains a derivation of Lifshitz's equation for dielectric materials and some of its properties. For instance, it is shown that Lifshitz's equation is equal to Casimir's result in the ideal metal regime. Lastly, there is a brief description of a theoretical formulation that has been used to correct the Casimir force model for plate's roughness and their finite conductivity. This formulation will provide a more realistic model for the Casimir force, hence reducing the accuracy of the experimental measurements.

2.1 Casimir Force for Ideal Metals

To obtain the Casimir force for two semi-infinite parallel plates at T = 0, it can be assumed that they are made out of ideal metal ($\varepsilon(\omega) \rightarrow \infty$) and electrostatically neutral. This defines the boundary conditions for the EM field fluctuations - the quantum vacuum fluctuations- between the plates. These fluctuations have an energy equivalent to the ground state's zero point energy of a quantum harmonic oscillator. Hence, for monochromatic fluctuations this energy is $E_\omega = \hbar\omega/2$. This means that the total zero-point energy between the parallel plates separated by a distance d, and both with side

dimensions of $L_x = L_y = L$, is the following:

$$E(d) = \sum_{l,m,n}{}' 2\frac{\hbar\omega_{l,m,n}}{2} = \sum_{l,m,n}{}' \pi\hbar c\left[\frac{l^2}{L^2} + \frac{m^2}{L^2} + \frac{n^2}{d^2}\right]^{1/2}, \qquad l, m, n \neq 0. \tag{2.1}$$

This equation accounts for two independent polarizations of the field and avoids term repetition; -only one polarization is included when either index is zero: this is the reason for the prime at the summation.

To calculate the zero point energy outside the plates, a box with sides L_x, L_y, and L_z is considered. If these dimensions are taken to infinity, the zero point energy inside the box has the following expression

$$E(\infty) = \frac{L^2}{\pi^2}(\hbar c)\frac{d}{\pi}\int_0^\infty dk_x \int_0^\infty dk_y \int_0^\infty dk_z \left(k_x^2 + k_y^2 + k_z^2\right)^{1/2}, \tag{2.2}$$

where $k_x = {\pi l}/{L_x}$, $k_y = {\pi m}/{L_y}$, and $k_z = {\pi n}/{L_z}$. This energy is the equal to the energy outside of the plates.

For semi-infinite plates, $L >> d$, $U(d) = E(d) - E(\infty)$ is the energy to bring the plates from infinity to a distance d from each other,

$$U(d) = \frac{L^2\hbar c}{\pi^2}\left[\sum_n{}' \int_0^\infty dk_x \int_0^\infty dk_y \left(k_x^2 + k_y^2 + \frac{n^2\pi^2}{d^2}\right)^{1/2} - \frac{d}{\pi}\int_0^\infty dk_x \int_0^\infty dk_y \int_0^\infty dk_z \left(k_x^2 + k_y^2 + k_z^2\right)^{1/2}\right].$$

2.3

This expression, of two infinite quantities, can be reduced to a finite quantity through various renormalization procedures. Physically, however, this is possible because the metal plates set a natural cutoff frequency and the cutoff function can be chosen accordingly. This cutoff function considers that the metal plates are transparent to high frequency field fluctuations; which happens when the frequencies of these fluctuations are much larger than the plasma frequency of the metal substrate. The chosen cutoff function and Eq. 2.3, after some mathematical manipulation, result in an expression that does not depend on the cutoff frequency or this cutoff function. This result is the expression in eq. 2.4, the Casimir energy:

$$U(d) = -\left(\frac{\pi^2 \hbar c}{720 d^3}\right) L^2.$$

2.4

This expression and $F(d) = -\nabla U(d)$ yield the Casimir force of Eq. 1.1.

2.1.1 Proximity Force Approximation

Precise Casimir force experiments are performed in the lens-plate configuration; specifically, between a sphere and a plate. This configuration has resolved the issues related to maintaining two plates parallel. Its disadvantage is that there is not an exact theoretical expression for its Casimir energy. To overcome this, researchers have used the Proximity force approximation (PFA) [40] to compare their force measurements to the approximated expressions of the theory. This is an approximate method to calculate the averaged interaction energy between two curved objects separated, at their closest

point, by a distance z. To calculate this energy, each of these objects' surfaces is redrawn with infinitesimal planes, located along the surfaces, and following the curvature of each object. It continues by calculating the interaction energy between two of these planes, one from each object, and facing each other. The result is the interaction energy per unit area between these facing planes, $E_i(w)$, where w is the separation between them and the i denotes the i-th pair of planes. This procedure continues between pairs of planes for all the planes of the objects. The sum of all the corresponding $E_i(w)$ terms per pair is the total interaction energy between the two objects, V(z):

$$V(z) = \int_S E(w)dS. \tag{2.5}$$

S is the total surface involved in the calculation of V(z). This expression assumes that the interaction energy between non-facing planes is negligible and that z is small in comparison to the radii of curvature of the objects.

The expression in Eq. 2.5 yields the approximate value of the Casimir energy between a sphere of radius R and a plate separated by a distance d. The negative derivative of this value with respect to d is the Casimir force for the same configuration:

$$F_{sp}(d) = 2\pi R E^0_{pp}(d), \tag{2.6}$$

where $E^0_{pp}(d)$ is the Casimir energy between two semi-infinite plates of eq. 2.4.

The proximity approximation, developed by Derjaguin, has been successfully applied to many fields, especially, fields related to scanning probe microscopy (SPM). In

the Casimir field however, where precision has become paramount, researchers have contested PFA [41, 42]. This is because, for the sphere-plane configuration, it introduces a relative error of the order of d/R to the theory [43]. This result, obtained from dimensional considerations, is less than 0.01 in current experiments. A recent [44] experiment however, has estimated that this value is smaller than d/R. This result contradicts the extrapolated results of numerical calculations from Emig et al. [41] and Maia-Neto et al. [42] For ideal metal substrates, these researchers have claimed a correction of the order d/R beyond PFA. They estimated that d/R ~ 1.4, using parameters of current Casimir experiments.

Recently, using the scattering method, other researchers have computed the Casmir energy between a sphere and a plate for non-ideal metals at non-zero temperatures. They have obtained expressions for materials described with the Drude model [45, 46], the plasma model [45, 46], and their corresponding generalizations [46]. For d/R > 1, these expressions are analytical and show large deviations from the PFA. These researchers have obtained analytical expressions for the energy and numerically found strong correlations between temperature, dissipation, and geometry. In addition, they have found that their results are material dependent. For d/R < 1, this method can attain exact values for intense numerical calculations. That is, since the scattering method depends on a multipole expansion of the partial EM waves scattered from sphere-plate configuration, when the sphere plate distance is small, the amount of terms in the expansion is large. Hence, the accuracy of this method relies on the amount of terms form the expansion are included. Additionally, only analytical expressions (not tabulated data) can be used for

the material properties. Since there is not a consensus of the relative error introduced by PFA and an exact calculation has not been performed yet, this experimental study considers this error to be of the order of d/R.

2.2 Casimir Force for Dielectric Materials

Microscopic theories, such as Van der Waals forces for neutral atoms, were not able to reproduce the result of Casmir [7], eq. 1.1, between two parallel plates. They obtained the same distance dependence, but the numerical value is off by 20%. This disagreement is due to the assumption, within these theories, that the interaction of atoms occurs only between pairs of them. This assumption is correct for rarefied media, but not for dense macroscopic objects, where the interaction between pairs of atoms is modified by the surrounding medium. To account for this, Lifshitz developed a macroscopic formalism that considers the interaction between objects through the fluctuating EM fields that are inside of them and leak outside of their boundaries [12]. These fields must be consistent with the dispersion relations of the medium and the boundary conditions of the objects. The result is an expression, referred to as Lifshitz's formula, which calculates the Casimir force between two dielectric plates at non-zero temperature. For the case of ideal metal plates at T = 0, it recovers the result of Eq. 1.1, and for rarefied media, at T = 0 as well, it yields the result obtained with microscopic theories.

Lifshitz's formalism has been revisited by many researchers [13, 30], which have obtained equivalent results with different and more modern formalisms, and not always explicitly recurring to the zero-point energy between the plates. Some of these

formalisms use Source theory [47], Green functions derivations and an approach based on the delta-functions potentials [30]. In this manuscript, Lifshitz's formula is obtained using the approach of Milonni [7]on the results by Van Kampen et al. [48], which, including retardation, and effectively calculates the zero-point energy between two dielectric plates. This approach reproduces Lifshit'z formula for dielctric materials and is coherent with the quantum vacuum fluctuations picture of the Casimir force. Its disadvantage is that it does not consider the absorption of the material. That is, in this approach, the procedure to measure the energy between the dielectric plates assumes only real dielectric functions. Nevertheless, the result is the Lifshitz formula, which can be used for materials with absorption i.e. materials with complex $\varepsilon(\omega)$. The answer to this paradox relies on a special mathematical procedure. To be able to sum the modes between the plates, the calculations are performed in the complex plane. This results in the modes frequency $\omega \rightarrow i\xi$, hence $\varepsilon(\omega) \rightarrow \varepsilon(i\xi)$, a quantity that is always real and obtained with the Kramers-Kronig dispersion relation. This connects the value of the dielectric function $\varepsilon(i\xi)$ to the non-zero absorption of the material. While the approach of Milonni is not entirely rigorous, since it contains certain mathematical weaknesses, researchers have shown that it can be corrected. Barash and Ginzburg gave a formal derivation of Lifshitz's formula in the context of zero-point fluctuations [7]. But most importantly, their theory assumes the dielectric functions to be complex, which means it includes the imaginary term of the permittivity related to the absorption of the materials.

2.3 Lifshitz's Equation by Van Kampen et al.

To obtain the Casimir force between dielectrics plates, they consider three parallel layers of different dielectric media. In this approach, these layers are characterized by their non-local responses to fluctuating EM fields, $\varepsilon_j(\omega)$. A schematic drawing of the configuration of the system under study is presented in Fig 1. The distance d between the

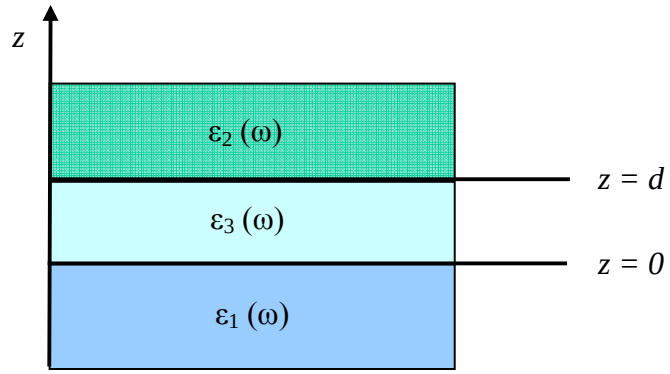

Figure 2.1. The system under study consists of three semi-infinite layers of three different dielectric media.

exterior layers is small in comparison with the dimensions of the other 2 layers. The fields inside each of the layers are described by the Maxwell equations without sources. They are uniquely defined with the boundary conditions of this configuration, which are the standard conditions for stratified media.

The EM fields in these configurations have a different solution in each dielectric region, a periodic solution in the region between the plates ($0 < z < d$), and exponentially decaying fields in the other regions ($z < 0$, $z > d$). Since the layers are semi-infinite only the z-component of the EM fields $E_z(z)$ is meaningful to the Casimir problem:

Eqs. QQ1

$$E_z(z) = Ae^{K_1 z}, \quad z < 0,$$

$$= Be^{K_3 z} + Ce^{-K_3 z}, 0 < z < d,$$

$$= De^{-K_2 z}, \quad z > d,$$

where $K_j = \sqrt{k^2 - \varepsilon_j(\omega)\,\omega^2/c^2}$, a real value, and A, B, C, and D are constants. These constants and the continuity conditions at the boundaries define the frequencies of the EM fields in the three regions. The frequencies are the solutions of the following expressions:

Eqs. QQ2

$$\frac{(\varepsilon_3 K_1 + \varepsilon_1 K_3)(\varepsilon_3 K_2 + \varepsilon_2 K_3)}{(\varepsilon_3 K_1 - \varepsilon_1 K_3)(\varepsilon_3 K_2 - \varepsilon_2 K_3)} e^{2K_3 d} - 1 = 0,$$

Eqs. QQ3

$$\frac{(K_1 + K_3)(K_2 + K_3)}{(K_1 - K_3)(K_2 - K_3)} e^{2K_3 d} - 1 = 0,$$

where eqs. QQ2 corresponds to the Transverse Magnetic modes (TM) and eqs. QQ3 to the Transverse Electrical modes (TE).

The zero-point energy associated with the frequencies, the solutions, of eqs QQ2 & QQ3, for the TM and TE polarizations is,

Eq. QQ4

$$E(d) = \frac{\hbar}{4\pi} A \int_0^\infty dk k \left[\sum\nolimits_N \omega_N^{TM}(k) + \sum\nolimits_N \omega_N^{TE}(k) \right],$$

where k is the wavenumber of the continuous modes and A is the area of the layers. In

this expression the modes in the x and y direction are continuous and therefore integrated.

The sums in eq. QQ4 are over the frequencies that satisfy eqs. QQ2 & QQ3. If these equations are defined in the complex ω plane as $F_{TM}(\omega)$ and $F_{TE}(\omega)$ respectively, the sums in eq. QQ4 are the sums of the zeros of these functions. A feature of these functions is that their poles do not depend on the distance d. In terms of these functions and using the Argument Principle of Complex Analysis, eq. QQ4 can be expressed in this form,

Eq. QQ5

$$E(d) = \frac{\hbar}{4\pi} A \left(\frac{1}{2\pi i}\right) \int_0^\infty dkk \left[\oint_C \omega \frac{F'_{TM}(\omega)}{F_{TM}(\omega)} d\omega + \oint_C \omega \frac{F'_{TE}(\omega)}{F_{TE}(\omega)} d\omega \right],$$

where the contour C is over the imaginary axis and a semicircle in the right half of the ω-plane. $F'_{TE}(\omega)\ and\ F'_{TE}(\omega)$ are derivatives with respect to ω of the functions defined above. It is assumed that the frequencies of eq. QQ4 are real, setting the values of ε_j (ω) to be real. Since the integral over the semicircle of C does not depend on d, the integral is performed along the imaginary axis. It is in this step that $\omega \rightarrow i\xi$. If a new function $G(\xi) = F(i\xi)$ is defined, eq.QQ5 reads,

Eq. QQ6

$$E(d) = \frac{\hbar}{8\pi} A \int_0^\infty dkk \left[\int_{-\infty}^\infty d\xi\ log\ G_{TM}(\xi) + \int_{-\infty}^\infty d\xi\ log\ G_{TE}(\xi) \right].$$

The force then, is,

Eq. QQ7

$$F(d) = -\frac{\hbar}{2\pi^2} A \int_0^\infty dk k \int_0^\infty d\xi K_3 \left[\frac{1}{G_{TM}(k,\xi)} + \frac{1}{G_{TE}(k,\xi)}\right].$$

With the purpose of showing the equivalence of this equation with Lifshitz's formula, this approach requires the introduction of the variables p, s_1, and s_2. In terms of the variables from eq. QQ7 have the form:

Eq. QQ8

$$k^2 = \varepsilon_3(i\xi)\frac{\xi^2}{c^2}(p^2 - 1), \qquad K_3 = \sqrt{\varepsilon_3(i\xi)}\frac{\xi}{c}p, \qquad K_{1,2} = \varepsilon_3(i\xi)\frac{\xi^2}{c^2}s_{1,2}^2.$$

Milonni has shown the equivalence between eq. QQ7 and Lifshitz's formula:

Eq. QQ9

$$F(d) = -\frac{\hbar}{2\pi^2} A \int_1^\infty dp p^2 \int_0^\infty d\xi \xi^3 \varepsilon_3^{3/2} \left(\left[\frac{\varepsilon_3 s_1 + \varepsilon_1 p}{\varepsilon_3 s_1 - \varepsilon_1 p} \frac{\varepsilon_3 s_2 + \varepsilon_2 p}{\varepsilon_3 s_2 - \varepsilon_2 p} e^{2\xi p\sqrt{\varepsilon_3} d/c} - 1 \right]^{-1} \right.$$
$$\left. + \left[\frac{s_1 + p}{s_1 - p} \frac{s_2 + p}{s_2 - p} e^{2\xi p\sqrt{\varepsilon_3} d/c} - 1 \right]^{-1} \right).$$

This expression is reduced to the case that Hendrik Casimir calculated when $\varepsilon_{1,2}(\omega) \to \infty$ and $\varepsilon_3(\omega) = 1$, which is the ideal metal limit, substituting these values in eq. QQ9, the force between the layers is,

Eq. QQ10

$$F(d) = -\frac{\hbar}{2\pi^2 c^3} A \int_1^\infty dp p^2 \int_0^\infty d\xi \xi^3 \frac{2}{e^{2\xi p d/c} - 1} = -\frac{\pi^2 \hbar c}{240 d^4} A.$$

In addition, Eq. QQ9 is useful to derive the retarded and non-retarded limits of the force between the plates, as well as the forces between neutral atoms, the commonly known

Van der Waals force.

To account for realistic properties of the dielectric layers and compare eq. QQ9 to experimental results, it is necessary to include certain corrections, some of which are addressed in the following section.

2.3.1 Corrections to the Model: Roughness and Finite Conductivity of the Plates.

Roughness and finite conductivity corrections increase the accuracy of the models of the Casmir force and reduce deviations between the models and their experimental counterpart. Finite conductivity corrections account for 10-20% of the force at d < 1 micrometer [43], and depending on the substrate's quality, the roughness can sufficiently change the force at short distances. Experimentally, this was first demonstrated by Mohideen et al. [21], where they were able to discern between the corrected model and the model predicted for perfect plates. In their study, the corrected model assumes that the corrections are not correlated. That is, the corrected expression of the Casimir force considers each correction separately as a multiplication factor. While this approach proves that the corrections have a measurable effect on the force, up to 20% due to surface roughness, it has shown that at short separations they can be correlated. For this reason, Klimchitskaya et al. [49] developed a non-multiplicative approach to account for the combined effect of conductivity and roughness corrections. Based on the Proximity Force Approximation, this approach geometrically averages the forces between surface features of the plates. Specifically, each force is calculated between two facing features of the plates and in the average, each force is weighed by the probability of having such a combination of features. This approach has been the method of choice for researchers

because current experiments measure the force at distances about a 100 nm, where the correlation of the corrections is more significant.

Nonetheless, the assumption in the experiment of this manuscript is that the corrections are not correlated. This experiment measures the Casimir force at separations above 120 nm for substrates with roughness of about 1 nm. It has been shown [50] that for such small roughness and separations, the approach used by Mohideen et al. yields equivalent results to the non multiplicative approach.

2.3.2 Conductivity Correction: Imperfect Conductivity of the Plates.

An imperfect conductor has a finite electrical conductivity, which is in contrast to the infinite conductivity of a perfect metal. Conductivity is considered in the Casimir force picture through the permittivities, $\varepsilon_j(\omega)$, of the dielectric layers in eq. QQ9. For the case in which two conducting plates, made of the same material, are separated by a vacuum gap, $\varepsilon_{1,2}(\omega) = \varepsilon(\omega)$ and $\varepsilon_3(\omega) = 1$. The choice for $\varepsilon(\omega)$, as mentioned above, will set the degree of realism of the theoretical model of the plates. However, inspection of the Lifshitz's formula shows that the model is effectively preselected. The reasons are that the force between the plates is measured at distances of the order of micrometers and that the dominant frequencies in this configuration are near $\omega \sim c/d$. Consequently, these frequencies are in the optical and infrared range. The plates' response to EM fields of these high frequencies is accurately described with the Plasma model for metals. In the context of the Lifshitz's formula ($\omega \rightarrow i\xi$), it has the following expression:

Eq. WW1

$$\varepsilon(i\xi) = 1 + \frac{\omega_p^2}{\xi^2},$$

where ω_p is the plasma frequency of the metal plates:

Eq. WW2

$$\omega_p^2 = \frac{4\pi N e^2}{m^*}.$$

In this expression, N is the density of conduction electrons and m^* is their effective mass.

To calculate the conductivity correction in the plasma model regime, researchers use a perturbation method that expands the force in powers of the relative penetration depth δ_0/d of the field fluctuations [43, 51], where $\delta_0 = {2\pi c}/{\omega_p}$ is the skin depth of the metal plates. For $d \geq {2\pi c}/{\omega_p}$, this approach is accurate and in good agreement with numerical results using optical tabulated data for the complex permittivity of the constituent material of the plate. Currently, researchers [13] have calculated the force for an imperfect conductor up to the fourth power of δ_0/d:

Eq. WW3

$$F_{pp}^c(d) = F_{pp}^0(d)\left[1 - \frac{16}{3}\frac{\delta_0}{d} + 24\frac{\delta_0^2}{d^2} - \frac{640}{7}\left(1 - \frac{\pi^2}{210}\right)\frac{\delta_0^3}{d^3} + \frac{2800}{9}\left(1 - \frac{163\pi^2}{7350}\right)\frac{\delta_0^4}{d^4}\right],$$

where $F_{pp}^0(d)$ is the expression in eq. 1 for perfect plates, and the superscript c refers to the force corrected for finite conductivity. Note that, at first order, eq. WW3 is congruent with the idea of the plates having a finite conductivity. That is $F_{pp}^c(d) < F_{pp}^0(d)$. Similarly, Lambrecht et al. [52] [53]found that the force between perfect mirrors is always greater than the force between mirrors with and arbitrarily-frequency dependant reflectivity.

Since experimental measurements are between a sphere and a plate, using PFA, the corresponding Casimir force with conductivity corrections is

Eq. WW4

$$F_{sp}^{c}(d) = F_{sp}(d)\left[1 - 4\frac{\delta_0}{d} + \frac{72}{5}\frac{\delta_0^2}{d^2} - \frac{320}{7}\left(1 - \frac{\pi^2}{210}\right)\frac{\delta_0^3}{d^3} + \frac{400}{3}\left(1 - \frac{163\pi^2}{7350}\right)\frac{\delta_0^4}{d^4}\right].$$

$F_{sp}(d)$ is the force between a sphere and a plate for perfect conductors of eq. 2.6.

2.3.3 Roughness Correction

Roughness of the plates in the Casimir force context has been a subject of continuous interest. There are two kinds of roughness, periodic and stochastic. Currently, there is much enthusiasm regarding roughness as a periodic corrugation of the plate, where exact formulations for the Casimir force for this configuration have been obtained [53, 54]. The researchers developing these models are interested in the diffraction-like effects of the zero-point fluctuations and the non-additivity of the force [53]. These effects occur when the corrugation period λ is smaller than the separation between the substrates d; otherwise, they are negligible. The study of these effects was triggered by an experiment, in which $\lambda/d > 1$, of Mohideeen et al. [55] It did not observe the mentioned effects, but showed that there exist a non-trivial boundary dependence of the Casimir force between a metal-coated sphere and metal-coated grating. In a recent experiment, Chiu et al. [56] precisely measured these effects between corrugated plates. However, when the Casimir force is measured between relatively flat surfaces,

diffraction-like effects due to the stochastic roughness is negligible, if the amplitude is less than 1 nm for separation distances >100 nm. This is the case of the experimental study reported in this manuscript. Although periodic features are found on the surface of the plates, the value of the corresponding correction is negligible as well. The reason is that the correlation length of these features is much bigger than the distance between the plates.

The roughness of the plates in the experimental study reported in this manuscript is modeled with a pairwise summation approximation [10], a phenomenological approach, and a simpler method. This approximation assumes that the interaction between two objects is the sum of the interactions between pairs of infinitesimal volumes; three or more infinitesimal volumes interactions are not consider. While Mohideen et al. [21] followed the same approach, the following description includes correction terms of higher order, and the roughness of each substrate considered. In this model, the roughness of the two surfaces is described by two different functions:

Eqs. XX

$$z_1 = \delta_1 f_1(x_1, y_1) \text{ and } z_2 = d + \delta_2 f_2(x_2, y_2).$$

Where δ_i is the rms variance of the surface features of the i-th substrate and the value d is the mean value of the distance between the plates. Moreover, for stochastic surface roughness on the plates the functions $\{ f_i(x_i, y_i) \}$ for i = 1, 2, form a distribution with δ_i^2 as its width. The distribution is normalized to one and $\delta_i < d$. This means that the Casimir energy between substrates, in the PFA approach, has to be averaged over all

possible values of the ith functions for each substrate. This is achieved assuming that the mentioned distribution is a normal distribution. Then, the Casimir force between plates, F_{pp}^{r}, is

Eq. XX1

$$F_{pp}^{r} = -\frac{1}{4A^2}\frac{\partial}{\partial d}\langle\langle U^{r}(d)\rangle_1\rangle_2,$$

where, A is the area of the plates and the superscript r denotes that the roughness corrections are included in the force. $U^{r}(d)$ is the Casimir energy, obtained through pairwise summation, of an induced dipole-dipole interaction. In addition, it approximately considers the non-additivity of the interaction.

For a sphere-plate configuration, eq. XX1 yields a Casimir force equal to,

Eq. XX2

$$F_{sp}^{r}(d) = F_{sp}(d)\left(1 + 6\left[\left(\frac{\delta_1}{d}\right)^2 + \left(\frac{\delta_2}{d}\right)^2\right] + 45\left[\left(\frac{\delta_1}{d}\right)^2 + \left(\frac{\delta_2}{d}\right)^2\right]^2\right),$$

where $F_{sp}(d)$ is the Casimir force between a sphere and a plate for perfect conductors, the expression in eq. 2.6.

To obtain a numerical correction from eq. XX2, the rms variance, δ_i, of each substrate is calculated with values measured from the topography of the substrates, which is generally obtained with an atomic force microscope. The topography is then, characterized by a probability distribution, where $v_i(h_i)$ is the probability of having an area of the substrate with features of height h_i. For a discrete number of v_i values, the average distance H_0 is,

Eq. XX3

$$\sum_{i=1}^{n}(H_0 - h_i)v_i = 0,$$

where n is the number of areas that are obtained in the analysis of the topography. With this same distribution the rms variance is,

Eq. XX4

$$\delta_{rms}^2 = \sum_{i=1}^{n}(H_0 - h_i)^2 v_i.$$

This expression and eq. XX2 yields the roughness correction to the Casimir force between a sphere and a plate in the pairwise approximation, both of which have a stochastic roughness.

The expressions obtained in this chapter are an initial approach to the description of the Casimir force between parallel plates and between a sphere and a plane. In eq. QQ9, Lifshitz, formula, the corrections due to surface roughness, eq. XX2, and the correction due to finite conductivity, eq. WW4, create a robust formulation that allows researchers to better compare their experimental results with the theory. However, since experiments are performed at non-zero temperatures, it is necessary to include the temperature in the formulism described above. Next chapter presents a derivation of the Lifshitz equation that includes temperature, as well as its results when different permittivities are employed.

3 Casmir Force at Finite Temperatures.

In this chapter, the Lifshitz's equation is considered for finite temperatures, and in this context, some of the consequences of the nature of the material of the confining plates are reviewed. In the first section, using the results from chapter two, the Lifshitz's equation for finite temperatures is derived. The following section describes controversial issues related to the thermal corrections of the Casimir force. The Lifshitz's equation is calculated for the competing models for the metal plates. The models considered are Plasma-type models and Drude-type models. To illustrate the controversies of these two approaches, this chapter ends with some arguments in favor and against these competing approaches.

3.1 Casmir Force for Two Parallel Plates at Finite Temperatures.

An intuitive, Casmir-like, way to understand the temperature dependence of the Lifshitz's equation, eq. QQ9, is to extend it by including thermal photons. In contrast to zero-point photons, thermal photons are the black body photons which result from the plates and surroundings being at non-zero temperature. This means that the energy of the EM fluctuations inside the cavity formed by the plates correspond to the solution to the Maxwell equations without sources. That is, $E(d) = \sum_l \hbar\omega_l\big(1/2 + n(\omega_l)\big)$, where $n(\omega_l)$ is the average number of thermal photons inside the cavity with frequency ω_l, given by the Planck formula, and the other term corresponds to the zero-point energy of the quantum fluctuation with the same frequency, as it was presented in eq. QQ9. Then, the total energy of the EM field fluctuations inside the cavity is,

Eq. 3.1

$$E(d) = \sum_l^* \hbar\omega_l \left(\frac{1}{2} + \frac{1}{e^{\hbar\omega_l/k_B T} - 1}\right) = \sum_l^* \frac{\hbar\omega_l}{2}\left(\frac{e^{\hbar\omega_l/k_B T} + e^{\hbar\omega_l/k_B T}}{e^{\hbar\omega_l/k_B T} - e^{\hbar\omega_l/k_B T}}\right)$$

$$= \sum_l^* \frac{\hbar\omega_l}{2} \coth \frac{\hbar\omega_l}{2k_B T}.$$

Where the middle expression was multiplied by

$$\frac{e^{-\hbar\omega_l/2k_B T}}{e^{-\hbar\omega_l/2k_B T}},$$

and k_B is the Boltzmann constant and T the temperature. The superscript* on the sum of eq. 3.1 means that two polarizations are included and should not include terms that are repeated, in a similar fashion to eq. QQ9. Eq. 3.1 is valuable because it makes a clear connection with the thermal photons through the Planck distribution, $n(\omega_l)$, in the same context as the Casmir's calculation. That is, conceptually, it helps understand the temperature dependence of the Casmir force. Since this is a Casmir-like approach to describe the Casmir force at non-zero temperatures, it is more appropriate to use methods, such as Lifshitz-type method, that include the nature of the material of the plates to calculate the temperature dependence of the Casmir force.

Since Lifshitz's 1956 paper [12], there have been many formal derivations of the Lifshitz's equation that include the temperature dependence. To obtain it, researchers have used different approaches. For instance, they have used source theory, scattering theory, quantum statistical physics, quantum field theory in the Matsubara formulation, etc [57]. Milonni's approach [7] is based on a symmetrical ordering of field operators, where an explicit contribution from the vacuum fields is found –This is a sourceless

theory equivalent to the known source theory of Swinger et al. [7]. Using eq. QQ7 and $\xi = -i\omega$ in Milonni's approach, the Casmir force between two plates of the same material ($\varepsilon_1 = \varepsilon_2 = \varepsilon$) and with vacuum in between ($\varepsilon_3 = \varepsilon$) is given by,

3.2

$$F(d) = -\frac{\hbar}{2\pi^2 c^3} A \int_1^\infty dp p^2 \int_0^\infty d\omega \omega^3 \left(\left[\left(\frac{s + \varepsilon p}{s - \varepsilon p} \right)^2 e^{-2\omega i p d/c} - 1 \right]^{-1} + \left[\left(\frac{s + p}{s + p} \right)^2 e^{-2\omega p d/c} - 1 \right]^{-1} \right) \coth \frac{\hbar\omega}{2k_B T},$$

where

$$s = \sqrt{p^2 - 1 + \varepsilon(\omega)}, \quad \text{and} \quad \varepsilon = \varepsilon(\omega).$$

Where the hyperbolic cotangent term from eq. 3.1 is present in the latter expression, this remarks, as is mentioned above, that the thermal photons and virtual photons are included in this expression. To account for these photons, eq. 3.2 has to be integrated over a range of real frequencies. This integral is better calculated in the complex plane, such that $\omega \rightarrow i\xi$, because the Argument Principle can be used. For this purpose, it is worth noting that the hyperbolic cotangent term has poles on the imaginary axis at,

3.3

$$\omega_n = 2\pi i n \frac{k_B T}{\hbar} = i\xi_n,$$

for all integers n. Note that the frequencies ξ_n are commonly referred as Matsubara frequencies. To solve the integral a contour is chosen on the top-right quadrant of the plane, in this way the poles in the imaginary axis are the only terms that contribute to the integral. eq 3.1 then, can be written as,

3.4

$$F(d) = -\frac{k_B T}{\pi c^3} A \int_1^\infty dp p^2 \sum_0^\infty{}' \xi_n{}^3 \left(\left[\left(\frac{s + \varepsilon p}{s - \varepsilon p} \right)^2 e^{2\xi_n p d/c} - 1 \right]^{-1} \right.$$

$$\left. + \left[\left(\frac{s + p}{s - p} \right)^2 e^{2\xi_n p d/c} - 1 \right]^{-1} \right).$$

The prime on the summation of eq. 3.4 indicates that a factor of ½ must multiply the n = 0 term.

A less intuitive yet more computationally useful approach to obtain eq. 3.3 is the thermal Green's functions method. The thermal green functions of eq. QQ7 are $G_{TM}(k, \xi)$ and $G_{TE}(k, \xi)$, which are periodic in imaginary time and have a period of $1/k_B T$ [58]. This means that instead of an integral over the frequencies ξ in eq. QQ7, there is a sum over the Matsubara frequencies of eq. 3.3. This transformation can be formally expressed in the following way,

3.5

$$\frac{\hbar}{2\pi} \int_0^\infty d\xi \leftrightarrow k_B T \sum_{n=0}^\infty{}' ,$$

Where the double arrow means that the transformation can be performed in both directions and the prime on the summation has the same meaning as above. In addition, the continuous value ξ transforms into the discrete values ξ_n of the Matsubara frequencies. The reason eq. 3.5 is not entirely formal is that, for real materials, the dielectric properties may be different for non-zero temperatures from those for temperature equal to zero [13].

Nevertheless, from eq. QQ7 the Casmir force between two plates of the same material ($\varepsilon_1 = \varepsilon_2 = \varepsilon$) and with vacuum in between($\varepsilon_3 = \varepsilon$) for at non-zero temperatures is,

3.6

$$F(d) = -\frac{k_B T}{\pi} A \sum_{n=0}^{\infty}{}' \int_0^{\infty} k K_3 dk \left[\frac{1}{G_{TM}(k, \xi_n)} + \frac{1}{G_{TE}(k, \xi_n)}\right].$$

If transformation 3.5 is applied to eq. QQ9, the expression in eq. 3.4 is obtained, making both methods equivalent.

Eq. 3.6 can be represented in a more physically intuitive manner in terms of the Fresnel reflections coefficients calculated along the imaginary axis, where they are real. Using the same assumptions for the plates, as in the derivation of 3.6 and for the case where the plates are placed in vacuum, these coefficients can be represented in this way,

3.7

$$r_{TM}(k, \xi_n) = \frac{\varepsilon K_3 - K}{\varepsilon K_3 + K}, \quad \text{and} \quad r_{TE}(k, \xi_n) = \frac{K_3 - K}{K_3 + K}.$$

Where $K_3 = \sqrt{k^2 + {\xi_n}^2/c^2}$ and $K = \sqrt{k^2 + \varepsilon(i\xi_n)\,{\xi_n}^2/c^2}$. The expression in eq. 3.6 can be written as,

3.8

$$F(d) = -\frac{k_B T}{\pi} A \sum_{n=0}^{\infty}{}' \int_0^{\infty} k K_3 dk \left[(r_{TM}^{-2}(k, \xi_n) e^{2K_3 d} - 1)^{-1} + (r_{TE}^{-2}(k, \xi_n) e^{2K_3 d} - 1)^{-1}\right].$$

This expression is in terms of both two field polarizations and its respective reflections coefficients. Simple inspection of eq. 3.8 results in troublesome physical consequences.

Below, they are reviewed and analyzed briefly. Moreover, integration of eq. 3.8 over the separation distance results in the Casmir energy between two identical plates with vacuum in between and for finite temperatures. This result will be used below to find, in combination with the PFA, the force in the sphere-plate configuration.

The expression in eq. 3.8 along with a suitable electric permittivity, $\varepsilon(i\xi_n)$, are commonly used to calculate the Casmir force in the plate-plate configuration. While choosing a $\varepsilon(i\xi_n)$ does not seem to be challenging, since, as mentioned in chapter two, the contributing frequencies are in the optical and in the infrared range. The low frequency contribution on a first inspection of eq. 3.8 appears to be small. At low frequencies, there are two competing descriptions the Drude and Plasma models. It is generally accepted that the low frequency behavior of real metals are well described with the permittivity of the Drude model. Nevertheless, regardless of the permittivity used in the Lifshitz's equation, one has to asymptotically recover the Casmir force for ideal metals at large separation distances as the reflectivity of metals approaches ideal behavior for large wavelengths. Furthermore, the expressions found have to satisfy well established laws of physics.

3.1.1 Simple inspection of the Casmir Force.

For ideal metals $(\varepsilon \to \infty)$, inspection of the expressions in eq. 3.7 result in $r_{TM}(k, \xi_n) = 1$ and $r_{TE}(k, \xi_n) = 1$ for $n > 0$. For the Matsubara frequency corresponding to $n = 0$, $r_{TE}(k, \xi_n) = 0$. To avoid this discontinuity, Schwinger et al. [14] suggested that the limit $\varepsilon \to \infty$ be taken first on eq. 3.8, implying that $r_{TM}(k, \xi_n) = 1$ and $r_{TE}(k, \xi_n) = -1$, and after that the summation over the Matsubara frequencies should be performed.

This prescription –called Swinger's prescription- allowed expression in eq. 3.8 to obtain Casmir's ideal metal plate value at large separation distances and at T = 0. The mathematical constraint put by this prescription on the metal has been contested by many researchers [13, 32]. They have then, suggested other models that describe the metal plates more accurately. For instance, simple models for real metals have permittivities that depend on frequency as $\varepsilon(i\xi) \sim 1/\xi$, Drude-type models are one example of them. If substituted in eq. 3.7, in the limit of infinite conductivity, the same discontinuity for n =0 described above is found. On the contrary, models that are intuitively more suitable, such as Plasma-type models where $\varepsilon(i\xi) \sim \omega_p^2/\xi^2$, and where at the n=0 Matsubara frequency the reflection coefficients are,

3.9

$$r_{TM}(k, 0) = 1 \qquad and \qquad r_{TE}(k, 0) = -1,$$

when the limit $\omega_p \to \infty$. That is, the Plasma-type models recover the ideal metal case. These arguments should be sufficient to deter researchers from pursuing Drude-type models to describe the nature of the metal plates. However, the alternative claim, that real metals are not well described with the Plasma-type models, is a sound statement in their favor. It should also be pointed out that, at short separation between the plates, where the temperature correction for eq. 3.8 is minimal, the variation between the Drude model and the Plasma models is around 2% [59]. At larger distances, the variation of the results from these models is more pronounced.

Researchers have explored several options to find a suitable permittivity, one that describes the metal as accurate as possible, while at the same time satisfying the

somewhat hidden constraints imposed by the Lifshitz's equation. Since all explored models lead to different results for the thermal Casmir force [13], the models presented below are the ones that support the use of tabulated optical data. However, to keep an open mind on the controversies of the thermal Casmir force, the results from the Plasma model and the Drude model are presented as well.

3.2 Casmir Force with Metals Described by Plasma-Type Models.

3.2.1 Plasma Model and Lifshitz's equation.

The Plasma model, eq. 2.ww1, describes the response of the free electrons in the metals without taking into account their relaxation processes, neglecting free electron collisions.

If the role of the core electrons are neglected and the complete permittivity is represented by the Plasma model, to obtain the thermal Casmir force eq. 2.ww1 is substituted in 3.8 for $T \ll T_{eff}$, where $k_B T_{eff} = \hbar c/2d$, and using perturbation methods and expanding in powers of δ/d and T/T_{eff} , the force is,

3.10

$$F_{pp}^{p}(d) = F_{pp}^{0}(d)\left[1 + \frac{1}{3}\left(\frac{T}{T_{eff}}\right)^{4} - \frac{16}{3}\frac{\delta_0}{d}\left[1 - \frac{45\zeta(3)}{8\pi^3}\left(\frac{T}{T_{eff}}\right)^{3}\right] + \sum_{i=2}^{6} c_i \frac{\delta_0^i}{d^i}\right],$$

where $\zeta(z)$is the Riemann zeta function and the coefficients c_i are explicitly calculated in Bordag et.al [43]. This expression is correct for $^{2\pi c}/_{\omega_p} < d < 2\mu m$, which are the distances of interest for the experiment of this manuscript. Furthermore, for perfect conductors, $\delta_0 = 0$, this expression reproduces results from other researchers as well as

the T = 0 value.

For the sphere-plate configuration, using the same approach as above and the PFA, the force is,

3.11

$$F_{sp}^{p}(d) = F_{sp}(d)\left\{1 + \frac{45\zeta(3)}{\pi^3}\left(\frac{T}{T_{eff}}\right)^3 - \left(\frac{T}{T_{eff}}\right)^4 - 4\frac{\delta_0}{d}\left[-\frac{45\zeta(3)}{2\pi^3}\left(\frac{T}{T_{eff}}\right)^3 + \left(\frac{T}{T_{eff}}\right)^4\right]\right.$$
$$\left. + + \sum_{i=2}^{6} \tilde{c}_i \frac{\delta_0^i}{d^i}\right\}.$$

Where $\tilde{c}_i = 3c_i/(3+i)$ and $F_{sp}(d)$ is eq. 2.7. For the limit of perfect conductors $\delta_0 \to 0$, this expression reproduces the low temperature asymptotic behavior obtained with quantum field theories [60].

For high temperatures $T \gg T_{eff}$, (achieved at d = 6 μm for T =300 K) using a numerical calculations, the asymptotic expression for the Casmir force is [10],

3.12

$$F_{sp}^{p}(d) = -\frac{\zeta(3)}{4d^2} Rk_B T\left(1 - 2\frac{\delta_0}{d}\right).$$

Where R is the radius of the sphere and this the dominant contribution for this expression comes form the zero term of the Matsubara frequencies. For perfect conductors this value reproduces known expressions [14, 61].

3.2.2 Generalized Plasma-Like Model.

This model emerges due to the need to include measured features of the permittivity particularly the role of the core electrons into the calculation of the thermal

Casmir force. However the inclusion of many of these features, such as the effects of metal dissipation due to free electron collision, lead to the problems outlined above for the Drude model. This model then, avoids including those effects and remains with the idea that the conduction electrons are free of collisions. In this model, the effects of the core electrons are included. The reasoning is that since the plasma model cannot be used for distances larger than the plasma wavelength, to include absorption bands due to core electrons eq. 2.ww1 needs to be extended [62]:

3.13

$$\varepsilon_{gp}(\omega) = 1 - \frac{\omega_p^2}{\omega^2} + \sum_j \frac{g_j}{\omega_j^2 - \omega^2 - i\gamma_j\omega}.$$

Where a group of oscillators (with strength g_j, ω_j resonant frequency, and relaxation frequencies γ_j) with non-zero frequencies describes the core electrons and the free conduction electrons are described with the plasma model. The oscillator parameters are obtained from tabulated optical data. Note that in expression 3.13 the relaxation properties of the conduction electrons are not included. Moreover, to assure that this is not the case; researchers obtain the tabulated optical data [63] for the imaginary part of the permittivity and subtract from it the contribution from conduction electrons:

3.14

$$\mathrm{Im}\left[\varepsilon_{op}(\omega)\right] = 2n'(\omega)n''(\omega) - \frac{\omega_p^2\gamma}{\omega(\omega^2 + \gamma^2)}.$$

Where $n'(\omega)$ and $n''(\omega)$ is the real and imaginary part of the index of refraction of the metal plates respectively, γ is the relaxation parameter, and the subscript op signifies that

the quantity is obtained from optical tabulated data. The value is fitted with a function describing an assortment of oscillators. The results lead to the parameters of each of the oscillators. Using eq. 3.13 and the fitting parameters, the permittivity along the imaginary frequency axis can be found. Another approach is to use the values of eq. 3.14 in combination with Kramers-Kronig relations that correspond to the generalized plasma-like model, for this case:

3.15

$$\varepsilon(i\xi) = 1 + \frac{2}{\pi}\int_0^\infty \frac{\omega \mathrm{Im}\left[\varepsilon_{op}(\omega)\right]}{\omega^2 + \xi^2} d\omega + \frac{\omega_p^2}{\xi^2}.$$

Then, the permittivity along the imaginary frequency axis is obtained. These two approaches have been typically used to compute the thermal Casmir force [13].

The advantage of these two approaches is that they use optical tabulated data to obtain the electric permittivity.

3.3 Casmir Force with Metals Described by Drude-Type Models.

3.3.1 Drude Model and Lifshitz's equation.

The Drude model for the electric permittivity is a phenomenological theory that describes the movement of the conduction electrons through a background of positively charged ions. It assumes that under an external field the conduction electrons of the material will gain, on the average, a drift velocity. The conduction electrons have mechanisms that stop them from continually being accelerated, which is not the case for free electrons. Since the mechanisms are not well specified in the model, a relaxation

time τ that accounts for all those mechanisms is introduced. It is only in this time interval that the electron can move as a free electron. Using kinetic transport theory, it can be shown that the effect of introducing the time τ is a frictional damping term in the equation of motion for the momentum per electron. However, for high frequencies,$\omega\tau \gg 1$, the effects of the frictional term are minimized and the Plasma model is recovered. Even when the model is not rigorous and lacks depth, to certain extent, it explains the macroscopic electrical conductivity and the thermal conduction in metals. Hence, it should be a suitable choice for the permittivity of the metal plates. Yet as we pointed out in the simple inspection of eq. 3.8, its place in the Lifshitz's formulation is unclear.

The electric permittivity then, is described in the Drude model as,

3.16

$$\varepsilon_D(\omega) = 1 - \frac{\omega_p^2}{\omega\big(\omega + i\gamma(T)\big)}.$$

When this expression is substituted in eq. 3.8 [31, 64, 65], the high-temperature limit is exactly equal to one-half of the corresponding value for the ideal metals, regardless of the value of the conductivity used for the real metals [66]. This large difference obtained for separation distances of 6μm and T = 300K has never been achieved experimentally for plates in thermal equilibrium. The reason is that the Casmir force is minute in that region and the experiments do not have enough resolution.

For the case $T \ll T_{eff}$, the thermal correction for the free energy per unit area between two plates obtained with the Drude model, $\Delta_T \mathcal{F}^{(D)}(d, T)$, is given by,

3.17

$$\Delta_T\mathcal{F}^{(D)}(d,T) = \Delta_T\mathcal{F}^{(p)}(d,T) + \mathcal{F}^{(\gamma)}(d,T)$$

$$-\frac{k_B T}{16\pi d^2}\int_0^\infty ydy\left\{\ln\left[1-\left(\frac{cy-\sqrt{4d^2\omega_p^2+c^2y^2}}{cy+\sqrt{4d^2\omega_p^2+c^2y^2}}\right)^2 e^{-y}\right]\right\}.$$

With the condition that,

3.18

$$\gamma < \xi_l.$$

Where $\Delta_T\mathcal{F}^{(p)}(d,T)$ is the thermal correction for the free energy per unit area between two plates obtained with the Plasma model and $\mathcal{F}^{(\gamma)}(d,T) \sim \gamma(T)\ln(T/T_{eff})$. For metals with perfect crystal lattices eq. 3.17 is satisfied, but for imperfect metals, where the residual relaxation is never zero, the condition of 3.18 is not satisfied.

This thermal correction has been experimentally tested only once to date and shown to be inconsistent with the data. The results from the experiment by [36, 67] at d < 1μm have shown at a high a confidence level that the last term of eq. 3.17 is not correct, thus excluding a thermal correction due to the Drude model. In addition, this thermal correction has been used to calculate the Casmir entropy by Bezerra et al [68]. They showed that for perfect crystal lattices at $T = 0$, the Casmir entropy is different form zero. Their result for the entropy at $T = 0$ is given by

3.19

$$S^{(D)}(d,0) = \frac{k_B}{16\pi d^2}\int_0^\infty ydy\left\{\ln\left[1-\left(\frac{cy-\sqrt{4d^2\omega_p^2+c^2y^2}}{cy+\sqrt{4d^2\omega_p^2+c^2y^2}}\right)^2 e^{-y}\right]\right\}$$

$$= -\frac{k_B\zeta(3)}{16\pi d^2}\left[1-\frac{4c}{\omega_p d}+12\frac{c^2}{\omega_p^2 d^2}-\cdots\right].$$

The result of this expression is a negative value. Most importantly, this result has been the most controversial result that has been obtained from the Drude model, since the consequence is that the Third law of Thermodynamics is not satisfied [13, 32, 68]. To solve this issue researchers have made various modifications to the Drude model. For instance, they have included impurities in the Drude model [33-35], which would lead to a nonzero gamma at zero temperature, which in turn leads to zero entropy at zero temperature. The result of this approach is that the entropy abruptly jumps to zero from a negative value at $T<10^{-14}$K. However, the fact remains that perfect crystals (on which most condensed matter theory is based) would lead to negative entropy at zero temperature., The inclusion of the Drude model in the Lifshitz's equation and the consequences of this are still a current and highly debated subject.

3.3.2 Optical Tabulated Data and the Drude Model.

The reason to use optical tabulated data within the Drude approach is the same as in the Plasma model. That is, more information about the role of the core electrons is needed to calculate the Lifshitz's equation at high precisions. The optical data is the more complete source of information about the surfaces. In this case, however, the data for gold below energies of 0.125 eV is not available. To resolve this, researchers extrapolate

the optical data to lower frequencies using the Drude or Plasma model. Note that these frequencies are necessary in the Drude model. To find the extrapolations, they use the imaginary permittivity of the optical data, Im $[\varepsilon_D(\omega)]$, and the standard Kramers-Kronig relations to obtain the permittivity along the imaginary frequency. This permittivity still lacks the low frequency contribution. To obtain it, they use the following expression

3.20

$$\text{Im}\,[\varepsilon_D(\omega)] = \frac{\omega_p^2 \gamma}{\omega(\omega^2 + \gamma^2)}.$$

Where the plasma frequency and the relaxation parameters were previously obtained from the optical tabulated data. Researchers typically have used the room temperature parameters [13],

3.21

$$\omega_p = 9.0\text{eV and } \gamma = 0.035\text{eV}.$$

Researchers have compared the Drude model (eq. 3.16) results to the results obtained with the optical data in the Drude approach that extrapolates the low frequency behavior. That is, using a correction factor to the Casmir pressure due to each of these two approaches, at separations of d = 1μm the percent difference between these factors is 0.14%. At d = 200nm, 100nm, and 50 nm, the difference is 2.8%, 7.7%, and 16% respectively. Bordag et al. [13] attribute this increase to the Drude model of eq. 3.16 not considering the contribution of the interband transitions of the core electrons. This is in contrast to the optical data that takes them into account.

4 Experimental techniques to explore the Casimir effect.

This chapter describes some of the techniques that have been used to explore the Casimir effect. It presents some of the related accomplishments, advantages, and disadvantages. It is divided into three sections; the first one describes the static deflection method to measure forces with an atomic force microscope (AFM), followed by a section that describes an AFM's dynamic method to measure the gradient of the force. In the last section, a non-AFM system is briefly reviewed. Using a sphere-plate configuration, it has been used to indirectly, and precisely, measure the Casimir pressure between two plates.

From detecting small ensembles of nuclei [69], to atom-by-atom manipulation [70], scanning probe microscopy (SPM) has proven to be a field of enormous capabilities [71]. This type of microscopy, initiated with the Scanning Tunneling Microscope (STM) of G. Binning and H. Rohrer [72], encompasses a vast number of techniques, working under similar principles, yet with different objectives. These principles have allowed researchers to locally probe several types of surfaces in different environments, such as air, liquid, and ultra high vacuum [71, 73, 74]. In addition, they record dynamic information in real-time, allowing them to measure interactions that evolve in time, such as chemical reactions [73]. For the first time, these two powerful characteristics led to the resolution of atoms on surfaces, and currently, they have strongly influenced many areas of science, such as biology, chemistry, physics, and engineering [75]. Due to their working principles, SPM techniques have proven to be reliable, highly versatile, and relatively simple to manufacture for more than two decades [75]. For these reasons, SPM techniques are well suited for Casimir force measurements. Specifically, there are

techniques, such as Atomic Force Microscopy, which are capable of measuring forces with sub-nanoNewton resolution at distances in the submicron range [76].

4.1 Static Deflection Method

Roy and Mohideen were the first researchers to use the advantages of the AFM in the Casmir field [28]. They precisely measured the Casmir force in the sphere-plate

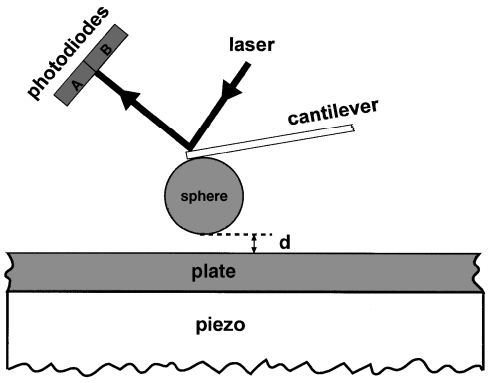

Figure 4.1. Schematic diagram of the experimental setup used to measure the Casmir force by Roy and Mohieden [1]. The difference between the signals from photodiode A and from photodiode B is proportional to the deflection of the cantilever. Note that, in Roy and Mohideen's experiment, the cantilever is modified by adding a metal-coated sphere. To maintain mechanical stability and to keep the modified cantilever electrically conductive, the cantilever is also coated with a metal.

configuration using the static deflection method, a closely related method to the AFM's Contact mode [73] for surface imaging. While in the latter method the distance between the probe and the investigated surface is kept constant, in the static deflection method, the probe-surface distance is linearly modified. In both methods, however, this distance is modified with a segmented piezoelectric tube. In contrast to the Contact mode, the deflection method results in a distance dependence of a force, which is exerted on the probe by the surface. The probe that detects this force is a cantilever specially designed to

bend in only one direction. This direction is perpendicular to the axis of the largest dimension of the probe. For Casmir force experiments, this is of the order of 10^2 μm, resulting in a cantilever's spring constant of the order of 10^{-2} N/m [77]. The bending of the cantilever results from Hooke's law in the linear limit and is the consequence, as mentioned above, of a resultant force exerted by the surface. Hence, decreasing cantilever's spring constant increases the force sensitivity of the AFM. The maximum attainable sensitivity is determined by the thermal noise driven oscillations of the cantilever [73]. The maximum force resolution reported in Casmir force experiments, using the static deflection method, is of the order of 0.5 pN [78]. A modified version of the static deflection method using lockin amplifier techniques has achieved a minimum sensitivity of 0.03 pN [23].

To detect the bending of the cantilever, most AFM systems use a laser that is focused on the free end of the cantilever and a segmented photodetector that captures the reflected light. When bending occurs, each photodetector senses a change in the laser intensity they receive. The difference between the signals from each detector is proportional to the deflection of the cantilever. Fig. 4.1 depicts Roy and Mohideen [28] schematic diagram of their experimental setup to measure the Casmir force using the static deflection method. The optical technique to detect its deflection and the sub-nanometer motion of the surface -key elements of the static deflection method- allowed researchers to precisely measure the Casmir force in the sphere-plate configuration.

This experiment was performed between an Al-coated sphere and an Al-coated substrate, resulting in an appreciable difference between the ideal metal model and the

experimental measurements. The authors concluded that the measurements needed to be compared to a more realistic model of the metal surface, one that included the finite conductivity and roughness of this surface. The success in their assumptions and the high resolution of the static deflection method led to a better understanding of the way virtual photons interact with real metals. Since these experiments, the static deflection method has been the experimental choice to explore the Casmir force, producing a plethora of achievements in the field [13]. For example, using this method, subsequent experiments on Au increased the precision and accuracy of the results and set the standard for various years [13]. In addition, to further the understanding of the interactions between virtual photons and real materials, they measured the Casimir force between a Au-coated sphere and a highly doped semiconductor [27]. These studies were performed with n-doped and p-doped semiconductors separately. The results were compared to the Lifshitz theory and good agreement was found. With similar experiments, the carrier density of the semiconductor was optically modified [23] using a chopped Argon laser and the lock in technique, as the increase in conductivity due to the absorption of light leads to variations in the reflection coefficients of the semiconductors on a large frequency range. This resulted in a modified force. The use of the lock in technique allowed a precision of 0.03 pN, which is an order of magnitude higher than the regular static deflection method. The results lead to the conclusion that for a consistent comparison to the theory, the dc conductivity of the silicon has to be neglected in the dielectric state. Another achievement of the static deflection method is in the study of diffraction-like effects in the Casmir field, where using a Au-coated sphere and Au-coated grating, recent

experiments have found a nontrivial boundary dependence of the force [55]. The large deviation found in the experiments could only be explained due to the force aligning the bottom of the sphere (the curvature provides a distance dependence) and along the corrugation of the grating. Furthermore, with a similar setup, except that the corrugations of the grating are imprinted on the Au-coated sphere, researchers used the deflection technique to find that the Casmir force is strongly dependant on the geometry of the boundaries. This force is called the Lateral Casmir force [22]. While the examples above were performed in high vacuum environments, the static deflection method has also been successful in measuring the Casmir force in liquid environments. Munday et al. [79] recently claimed to have measured a repulsive Casimir force between Au-coated sphere and a silica substrate immersed in a Bromobenzene solution. The results, while still debated [13], show the range of possibilities of the static deflection method in the Casimir field. Overall, this method has proven to be reliable and precise at small separations between the sphere and the plate, at distances < 500nm. However, its achievements have left many unanswered questions. Because some of these achievements were performed at the resolution limit of the deflection method, new high force resolution techniques, capable of measuring the force at separations of the order of micrometers, have the potential to resolve these questions. Additionally, many new phenomena appear at large separation distances.

Techniques that increase the force resolution at large distances could shed some light on the role thermal photons play in the Casimir effect. In addition, they might be able to resolve long-standing disputes about the influence that the material losses have on

this effect. Previous techniques that have attempted to resolve these issues were not successful [13]. Their resolution was not sufficient to detect these effects or their systematic errors were large. However, new techniques to measure the force have been attempted [36, 80]. Researchers have used methods from Dynamic Force microscopy (DFM) for this purpose. They have selected DFM over other techniques because of its success in other fields and essentially, because under certain conditions, it can detect forces of the order of sub-attoNewtons [81]. Since the minimum force attainable with the static deflection method is about 0.5 pN, this technique could potentially increase the force resolution by several orders of magnitude. While experiments using dynamic methods have not achieved the anticipated resolution, they have shown good progress. For instance, Decca et al. [2] have proved that a dynamic method, a similar version to the Frequency Modulation method for an AFM [71], is more sensitive than the static deflection method. Recently, using dynamic methods, their experiments have attained the smallest force resolution, being able to exclude certain thermal corrections to Lifhitz's equation due to the Drude model [36]. This achievement is a first step to resolving the polemic regarding the material losses in the Casmir effect at non-zero temperatures. Jourdan et al. [39] have also used a dynamic method to explore the Casimir effect. Using a similar setup to that of the authors of this manuscript, they measured the Casmir force gradient between a Au-coated sphere and a Au-coated plate at room temperature. However, the results of their experiments did not indicate unusual sensitivities or a high precision. Iannuzzi et al. [82], for example, have used a lock in based dynamic technique to compare the Casimr force gradient between a Au-coated sphere and Au-substrate

against the same sphere and a substrate made of highly-doped Indium Tin oxide (ITO) [83, 84]. They used a modified commercial AFM that measures the Casmir force gradient and the contact potential, V_0, directly and simultaneously. They measure the force effectively through a difference measurement and V_0 with a feedback loop that keeps the electrostatic force continuously compensated throughout the measurements. Even when this technique was able to resolve a 50% reduction of the force in the new investigated material, ITO, it measured this value at short distances, ~120 nm. At distances of about 200nm, the error in their measurements seems to be higher than 50%, leading to believe that their particular dynamic method is not fit to explore the Casmir force at large separation distances. Furthermore, the advantage of their technique then, seems to be solely the direct measurements of V_0, which is in contrast to the indirect process used by most researchers [13]. While various experiments have used dynamic techniques to explore the Casmir effect, their results have not had the force resolution to contribute to the understanding of the force at large distances and at non-zero temperatures. Since these techniques have already been successful in other fields, it is paramount that instruments that exploit the full potential of these techniques be used in the Casmir field. Below, the dynamic technique used in the apparatus reported in this study is described.

4.2 Dynamic Force Microscopy

When the AFM was invented c. 1986 [85], the microscopy community suggested various techniques, under the AFM working principles, to measure forces. [86] However, the simplicity of the static deflection technique made it an instant success and

consequently very popular [86]. At the same time, its highly local and enhanced resolution images in real time, which ultimately achieved atomic resolution [87], put other AFM techniques out of active consideration, at least for a limited time. Currently, many of the previously suggested techniques have attained similar results to those produced with AFM's static deflection, and some of them, became task specific. Such is the case of a DFM technique called Frequency Modulation (FM-AFM) [88]. One of the methods initially known as a non-contact mode attained atomic resolution two years after its static counterpart [89] and was originally conceived as a technique to explore short-range forces, even when a careful selection of the intrinsic properties of the cantilever allows it to be used for long-range forces. The sensing element of this technique is the change of resonant frequency of a periodically driven cantilever, where the change is proportional to the gradient of the force, while assuming that the amplitude of the oscillation of the cantilever is small in comparison to the range of the force. Paramount in this technique is that the driving frequency be kept near the resonance frequency of the cantilever, since the capability to detect frequency changes, with high signal to noise ratio, depends on this factor. To maintain that condition throughout the measurements, a feedback control adds every measured change in resonant frequency to the cantilever's driving frequency, allowing the sensitivity to be close to its highest value throughout the entire measurement. While in this method the force is not directly measured, there are mathematical procedures that calculate the force using the measured gradient [71].

The technique used in the instrument reported in this manuscript is a simpler version of the method described above. Unlike the FM method, the cantilever is not

periodically driven, but it is left to resonate in response to the thermal bath surrounding it. While the source of the cantilever oscillation is different, the outcome is nevertheless equivalent i.e., the change in resonant frequency of the cantilever is proportional to the force gradient. The change is measured with the resonant frequencies from the recorded resonance peaks with and without the force present. For this purpose, we use an FFT Spectrum Analyzer [90], an instrument that will automatically record the oscillations of the cantilever, Fourier Transform the collected data, and generate a resonance peak. In contrast to the FM method, the capability of detecting the change in frequency is dependent solely on the frequency resolution of the Spectrum Analyzer. This means that an increase in resolution will increase the measuring time. In addition, the detection system of this technique consists of one sole instrument, which reduces the experimental complexity of this method. Although theoretically and experimentally simpler, it is, conceptually, not less sensible than the FM method. Moreover, while the FM method requires being fine-tuned to achieve high signal to noise ratio (SNR), the method used in this study has a SNR defined by the Spectrum Analyzer and the signal's detection system. Simplicity drove this experimental study to choose this method over other more established methods, and while the method has disadvantages, they are relatively minimal when measuring the Casimir force. The latter will be described in detail in the next chapter. The method's theoretical approach is described below.

The dynamics of a thermally driven cantilever is described with the Langevin equation for a harmonic oscillator:

Eq. SS

$$\ddot{z} + \frac{\gamma}{m}\dot{z} + \omega_0^2 z = \frac{1}{m}G(t).$$

Where $\omega_0 = \sqrt{k/m}$ is the resonant angular frequency, k is the spring constant of the cantilever, γ is the damping coefficient, and G(t) is the stochastic force representing the thermal bath where the cantilever is immersed. The solution of eq. SS is a Lorentzian peak centered at ω_0 and a full width half maximum (FWHM) of *** [91]. The average oscillation amplitude is $\langle z \rangle = \sqrt{k_B T/k}$, which for the modified cantilevers is around 0.5 nm at T = 300 K. In the Casimir force context, the substrate will exert a force $F_{sp}(z)$ on the modified cantilever (it has a sphere attached to it and has gone through various processes to make it entirely electrically conductive), hence adding an external force to the RHS of eq. SS. If $F_{sp}(z)$ is represented in a Taylor series expansion; for small oscillations of the cantilever eq. SS reads,

Eq. SS1.

$$\ddot{z} + \frac{\gamma}{m}\dot{z} + \frac{1}{m}(k - k_{sp})z = \frac{1}{m}\left[G(t) + F_{sp}(z = 0)\right].$$

Where $k_{sp} = dF_{sp}(z)/dz$, that is, the equivalent of a sphere-plate spring constant is the gradient of the force between the sphere and the plate. Let $k_{eff} = k + k_{sp}$ be the effective spring constant and $\omega_{eff}^2 = k_{eff}/m$ the effective resonant (angular) frequency of the cantilever. Then, for $k \gg k_{sp}$

Eq. SS2

$$\Delta\omega = \omega_{eff} - \omega_0 = \frac{\omega_0}{2k}\frac{\partial F_{sp}(z)}{\partial z}.$$

The change in frequency is proportional to the force gradient. This expression is the basis of the technique used in this experimental study to explore the Casimir effect. An advantage of measuring the force gradient is that, using the Proximity Force Approximation (PFA) described in Chapter 2, specifically eq. 2.6, the Casimir pressure between two plates, $P_{\parallel}(z)$, is obtained.

eq SS3

$$P_{\parallel}(z) = \frac{1}{2\pi R}\frac{\partial F_{sp}(z)}{\partial z},$$

where R is the radius of the sphere.

Atomic force microscopy techniques, both static and dynamic, are powerful and simple techniques that have been proven to be well suited to explore the Casimir effect. Even though high precision measurements are experimentally challenging, to measure the Casimir force or its gradient, essentially the only experimental requirement is to modify the cantilever of an AFM. That is, a coated sphere has to be added to its free end to obtain a reasonably precise force measurement [92]. The rest of the AFM already has most of the components needed for a force measurement. For example, the optical detection system, for both the static and dynamic methods, has been originally devised to resolve minute changes of the sensing element. The plate motion, controlled with a piezoelectric tube, reaches sub-nanometer resolution and has a distance range larger than one micrometer. These features and the intrinsic properties of the cantilever were designed to

measure forces of the order of nanoNewtons [71], which is the magnitude of the Casimir force in the micrometer range. The AFM is not only experimentally ideal for force measurements, but also the theory of its operation is well established and robust. An example is the PFA, which had already been used to calculate force interactions between the tip of a cantilever and a substrate [71]. For Casimir force measurements between a sphere and a plate this approximation is essential. The simplicity and capability of these AFM techniques has made more people venture to measure the Casimir force with an AFM than with any other apparatus.[28, 79, 83, 93] It has been measured in air, vacuum, and most recently in liquid [79]. Another important factor is that AFMs are commercially available; they are simply modified and easily fabricated. Moreover, since more scientific achievements in the Casimir field have been produced with an AFM than with in any other apparatus, it would appear that the achievement payoff vs. simplicity ratio is larger for AFM techniques. This should indicate that they are a natural way to proceed in exploring the Casimir phenomena.

4.3 Non-AFM methods.

Exploring different techniques or different instruments could possibly generate new physical phenomena. Various instruments with different techniques were intended to explore the Casimir effect before high precision experiments were attempted. As was mentioned above, it was only then, that experiments were accurate enough to obtain physical insight into this effect. For this reason, attention is exclusively directed to non-AFM techniques that have been able to accomplish this goal. For instance, techniques

using Microelectromechanical devices (MEMS) have produced significant scientific achievements in the Casimir field [2, 3, 36, 44, 94] and recently, have been used to show the potential technological application of the force in the nanotechnology industry [24]. In contrast to the AFM methods, using MEMS is a more elaborate route, since they need to be fabricated in a nanofabrication facility and the force detection system requires finely tuned electronics. The MEMS technique has nevertheless proven to be an excellent way to measure the Casimir force. Using DFM methods, it has achieved better force resolution and slightly better precision than the AFM technique [36]. So far, it is the only technique, besides the AFM technique, that has achieved precision results of the order of ~1%. Due to its importance, we briefly describe this MEMS technique in the following subsection.

4.3.1 MEMS technique to measure the Casimir force.

For the exploration of the Casimir effect, researchers have used a micromachined oscillator, a type of MEMS that resembles a seesaw. A schematic diagram of an experimental setup that uses this oscillator is shown in fig. 2. The oscillator's lever is made of a highly doped polysilicon and the fulcrum is made up of two serpentine rings, one on each side of the lever, anchored to a Silicon platform that is covered with a Silicon nitride layer. From fig. 2 it is possible to distinguish a serpentine spring on the right hand side of the lever; for clarity, it is not shown to be anchored to the platform in the figure. The dimensions of the lever in Decca et al. [36] are 500µm X 500µm by 3.5 µm thick. Under the lever, and placed on each side of the fulcrum, there are two polysilicon electrodes. The distance between them and the lever is about 2µm. To measure the

Casimir force, researchers hold the oscillator close to a metal-coated sapphire ball that is epoxy glued to an Au-coated optical fiber, allowing their point of contact to be

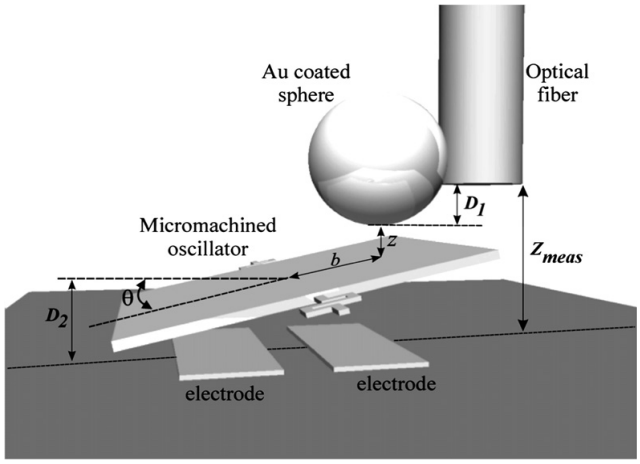

Figure 4.2. Schematic diagram of the experimental setup by Decca et al. [2] A similar design was used by Chan et al. [3].The relevant parameters of this setup are shown

electrically conductive. In addition, the radii of the balls that have been used with the micromachined oscillators are, for the most part, larger than in the AFM measurements. In Decca et al. [36, 67] the radius of the ball is R = 151.3μm, which is ~ 50% larger than the spheres used in the AFM experiments. It is worth noting that this experimental setup is more elaborate than the AFM setup, yet both have many similar features.

Micromachined oscillators (MO) have been used to explore the Casimir effect with two methods, a static deflection-type, and a dynamic-type. The sensing element of the former is the difference between the capacitance of each electrode and the lever, which is non-zero because of the alternating up and down motion of the lever due to a force, F(θ), exerted by the ball. In addition, this difference is proportional to the deflection angle θ of the lever, and since it is small, it is proportional to the force F(θ). As with the dynamic AFM techniques, F(θ), the force between a sphere and the lever is

not the quantity measured in the dynamic-type method. It is the force gradient $\partial F/\partial\theta$, which, using eq. SS3, can be utilized to obtain the pressure between two plates. In this method, the gradient is measured with the FM-AFM technique described above. The theoretical formulation is slightly changed to account for the instrumental differences. Since the sensing element of the MO is proportional to the deflection angle θ, the equation of motion of the lever is in terms of this angle. Any force exerted on the lever enters in the equation as a torque. Experimentally, the only differences are instrumental. The lever is periodically driven close to its resonant angular frequency by applying a periodic voltage on the electrodes below the lever. A force exerted on the lever produces a change in its resonant angular frequency. The difference $\Delta\omega_{MO}$ between the resonant angular frequency with a force ω_r and the one without ω_0 is proportional to the force gradient. For small oscillation amplitudes,

Eq SS4

$$\Delta\omega_{MO} = \omega_r - \omega_0 \; = \; -\frac{b^2}{2I\omega_0}\frac{\partial F_{sp}(z)}{\partial z}.$$

Where b is the lever arm of the oscillator, I is its moment of inertia, ω_0 is its resonant angular frequency at infinity, and ω_r is the effective angular resonant frequency of the oscillator. In addition, Eq. SS4 assumes that, if $\kappa = \omega_0^2 I$, is the torsional spring constant, $\kappa/b^2 \gg k_{sp} = \partial F_{sp}(z)/\partial z$. This expression is experimentally satisfied by the Electrostatic force and the Casimir force at the explored distance range.

The rest of the procedure for this technique is the same as the one described for

the FM-AFM technique.

Static and dynamic methods have successfully been used to study different properties of the Casimir effect, but not until the experiment by Decca et al. [95] have the two methods been compared in the Casimir field. Using a micromachined oscillator, they used the same experimental setup to quantitatively compare the static-type and dynamic-type method. They show that the latter method has two orders of magnitude more force resolution than its static counterpart. This result has provided researchers with evidence of the potential that dynamic-type methods have in the Casimir field. Currently, using a micromachined oscillator, several achievements have already been attained with these methods. For example, in the low temperature approximation and up to separation distances of 700 nm, they have been used to exclude the thermal correction due to the Drude model [36]. They reached this conclusion from a Casimir force room-temperature study between a Au-coated sphere and a Au-coated plate. In addition, to understand the role of conductivity in real metals, these researchers have measured the Casimir force between copper (Cu) and Au in the sphere-plate configuration [95]. The same team has explored possible corrections to the PFA in the same configuration [44]. Other authors, using similar setups [3], have measured non-linear behavior of a periodically driven micromachined oscillator caused by the Casimir force. More recently, Chan et al. [94] studied qualitatively the diffraction-like effects in the Casimir effect. They measure the force between a Au-coated sphere and a highly doped Si substrate with an array of nanoscale rectangular corrugations. All these examples demonstrate that dynamic methods have a vast potential in the exploration of the Casmir effect field.

5 Experimental Setup and Procedures

In this chapter, we present the most important features of the low-temperature atomic force microscope (AFM) that we designed and built to measure the Casimir force gradient in the sphere-plate configuration at different temperatures and as a function of distance. One of the most distinctive qualities of this microscope is its capability to precisely measure force gradients from 100 nm up to 2 μm in separation distance at 6 K and in a high-vacuum environment. We also present the calibrations and the procedures at 300 K, 77 K, and 6.3 K, which are the temperatures where we have successfully measured the force gradient. At these temperatures, the microscope's sensitivity allows us to measure the Casimir pressure for separation distances up to 800 nm.

The structure of the chapter is the following: In the first section of this chapter, we describe the design of the microscope, the cantilever fabrication, and the sample preparation. Section II describes the detection technique to measure force gradients. In section III, we present the magnetically damped system that keeps the microscope mechanically isolated from external vibrations. Section IV corresponds to the vacuum system as well as the cryogenic techniques we use to cool and keep the microscope at low temperatures throughout the measurements. In section V, we describe the LabView code that controls the microscope operations as well as the tasks to measure force gradients. Sections VI and VII discuss the grounding and the procedures to measure force gradients with this microscope respectively.

5.1 Main Design of the Instrument.

The instrument was designed mainly to precisely measure the Casimir force gradient at low temperatures and at large separation distances. It could potentially be used in the temperature range between 6.3K and 300K with maximum separation distances of 2 μm and 15 μm respectively. To achieve our purpose we built an AFM located at the end of an insert of a single-jacket Dewar capable of withstanding low temperatures and maintaining an interferometric cavity aligned from room temperature to 6.3K. The interferometric cavity is formed with the cleaved end of an optical fiber and the top free end of the microcantilever of the microscope. The random changes in the cavity length are correlated to the thermomechanical resonant frequency of the microcantilever, which, in the presence of a force, will be modified. The changes in its resonant frequency are detected with an interferometer-based-dynamic technique. As mentioned in chapter 4, a change in resonant frequency is proportional to a force gradient.

The motion of the substrate is controlled with a 3” segmented piezoelectric tube, this allows us to achieve large separation between the substrate and the sphere and a high degree of length resolution. To detect the relative motion of the substrate with respect to the cleaved end of an optical fiber, we use an interferometric displacement sensor that uses the same principle that the interferometer from the cantilever uses.

Reducing substrate contamination and mechanical coupling of the AFM to external vibrations is essential for precise Casimir pressure measurements. Consequently, the AFM is enclosed in a high-vacuum compatible container where it is suspended through a two-stage spring system that is magnetically damped. This container connects to an oil-

free vacuum system outside the Dewar through a stainless steel pipe that runs along the insert.

A picture of the atomic force microscope that we built is shown in Figure 5.1. Various parts of the microscope are indicated

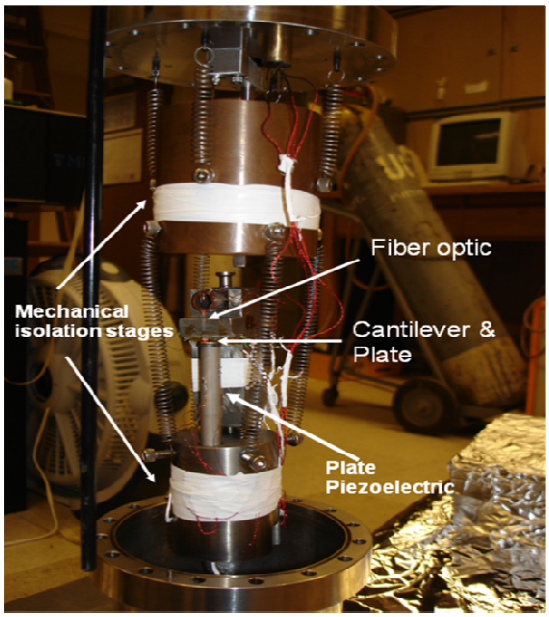

Figure 5.1. A picture of the atomic force microscope that has been used to measure the Casimir pressure at different temperatures. The two stage system is shown without the damping system. Note the segmented piezoelectric tube that controls the motion of the sample plate.

5.2 AFM construction.

To maintain the alignment of the cantilever/optical fiber cavity in a large temperature range is paramount, therefore our construction material of choice for the AFM is Molybdenum (Mo). This material has a low thermal expansion in the range between 5 K to 300 K, has good electrical conductivity [96, 97], and has been shown to be appropriate in similar instruments [97]. In comparison to similar low thermal expansion materials, its electrical conductivity improves the magnetic damping of the two-stage spring system

that holds the microscope.

The AFM consists of two parts: The microscope head and a cylindrical base where the head rests. Both parts contain important elements of the AFM: The head holds the modified Silicon (Si) cantilever and two optical fibers. The base holds the segmented piezoelectric tube that holds the Au coated sapphire plate. These two parts of the AFM are connected with a $1/80^{th}$ thread SS vented screw that goes through the head and four stainless steel (SS) compression springs that regulate the distance between the base and the head of the AFM, therefore controlling the coarse separation distance between the coated sphere and the plate. Note that the threads for the SS screw are only on the base, leaving the head loose. We address this by joining the head and the screw together with two retaining rings that are attached to the screw at the top and bottom of the head. To stop the head from rocking we put Teflon tape between the screw and the head. To stop it from rotating while still allowing it to slide in z-direction we attached two L-fixtures to the base. They are located on both sides of the head. These previous adjustments permit us to twist the head of the screw to move the microscope's head up and down while only changing the relative vertical distance between the head of the microscope and its base.

Since the interferometric cavity formed between the optical fiber and the cantilever has to be aligned for a large temperature range, the procedure we use to attach the modified cantilever and the optical fibers to the head of the microscope is essential. We describe then, the process to attach the cantilever and after that, the process to attach the fibers.

To attach the cantilever to the AFM’s head, we glue a chip with silver (Ag) epoxy on

to a custom Mo chip holder. The chip contains the modified cantilever. Note that commercial cantilevers come on the short length of small rectangular tablet or chip. This feature is useful for cantilever manipulation and particularly for our experiment; it allows us to thermally and electrically anchor the modified cantilever. Next, we screw in the chip holder to the AFM's head using a custom Mo clip. The chip holder sits on a small piezoelectric, capable of oscillating the cantilever and changing the length of the interferometric cavity. However, it cannot be used to align that cavity. All the alignment has to be done manually and before the AFM is in its high-vacuum container. That is, we cannot align the cantilever with the optical fiber once the container is closed.

The microscope has two optical fibers attached to its Mo head. One detects displacements of the cantilever and the other detects displacements of the Au substrate. The former is glued to the AFM head at only one spot with Stycast 2850-FT epoxy while the latter is glued near the former and at one spot with GE Varnish. We use epoxy on the one fiber because it has low thermal expansion in the temperature of our interest. In contrast, we use Varnish on the other, because as long as the cleaved fiber end is perpendicular to the large-area-Au substrate the interferometric cavity will exist. In addition, GE Varnish is useful because it is easily removable.

The base of the AFM contains a 3" segmented piezoelectric tube capable of moving in X, Y, and Z directions. The piezoelectric is glued to the Mo base with Stycast 2850FT. To reduce the length of the head of the AFM a third of the piezoelectric tube is inside the base through a vented hole. At the top of the piezoelectric tube, there is a Vespel [98] fixture to hold the Au substrate and electrically isolate its metallic segments. The

microscope is held by a two-stage spring system, this base is the bottom stage of the system.

5.3 Fabrication of the modified microcantilever.

This section is divided into three parts: the first one describes the preparation and certain modifications of the cantilevers, the second one describes the cleaning procedure of the spheres, and the last one describes the assembly of the modified cantilever. That is, a cantilever with a metal-coated sphere on the bottom of its free end. In addition, this sphere-cantilever microstructure goes through a process that assures a minimal electrical resistance between the coated sphere, the cantilever, and the chip corresponding to the cantilever.

5.3.1 Preparation and Modification of the Cantilevers.

We use commercial monocrystaline Silicon (Si) cantilevers [99] that are n-doped and have a specific resistance of 0.01 to 0.05 Ohm*cm. [99]We chose these cantilevers because their internal structure has only a small amount of internal stresses, in comparison to other materials like Silicon nitride (SiN_3). This implies that their energy dissipation is small, leading to a high quality factor (Q). From these types of cantilevers, we use the ones with the smallest spring constant (~0.03 N/m). Many times these cantilevers will have some defects on their surface that will increase the energy dissipation. Hence, we select the ones with the least amount of these defects. The chosen cantilevers are cleaned with high-purity acetone and then rinsed with distilled and deionized water (DDW). After that, the silicon dioxide (SiO_2) on the surface of the

cantilever is etched with a solution of Hydrofluoric acid for one minute. Finally, they are double rinsed in a solution of DDW. For the cantilevers to remain electrically conductive and free of dirt and debris, it is important to follow this recipe. If after the process these cantilevers are left for more than three hours, they might already be useless for our purposes. This is because a native layer of SiO_2 increases their resistivity and the sphere will not be electrically connected to the cantilever. Moreover, we have found that visible debris changes the Q of the cantilevers substantially, therefore, it is important to keep a clean environment while processing the cantilevers. Right after the cleaning and etching procedures, we solder Indium (In) to the sides of the chip that contains the cantilevers to increase the electrical conductivity throughout it. To minimize the resistivity between the cantilever and the Au coated sphere we repeat the cleaning and etching procedure just before attaching the hollow spheres to the cantilevers.

5.3.2 Cleaning Procedure of the Spheres.

To maximize the sensitivity of the AFM we use hollow-soda-lime-borosilicate-glass bubbles from 3M [100]. This choice allows the modified cantilever to have larger resonant frequencies, hence, as mentioned in chapter 4, higher resolution. Furthermore, these bubbles, on average, have few defects, have constant radii, and have removable debris. While these spheres are not ideal i.e. debris-free spheres that have fewer or no defects, we have not yet found a better choice in the market.

The sphere cleaning procedure removes debris, mostly broken pieces of spheres, and organic material. The first step of the cleaning process is to make a 10 ml solution of Ethanol or Isopropyl alcohol (IPA) with 1-2 ml of bubbles. This solution is thoroughly

mixed in a vortex mixer for about 1 minute. Then, using a pipette, the alcohol is extracted from the solution, leaving the solute, the bubbles, in the vial. To remove fiercely attached debris, we make a solution of 10 ml solution Hydrogen peroxide (H_2O_2) and the rest of the bubbles in the vial. Using a vortex mixer, the bubble solution is mixed for about 2 min, allowing the Oxygen released from the solution to remove debris from the bubbles. Once the solution is mixed, the H_2O_2 is extracted, leaving the bubbles to be rinsed with IPA or ethanol. To separate the debris from the bubbles, we centrifuge an alcohol/bubbles solution, (same ratio as the first alcohol solution), for 10 minutes. Finally, since there is debris and broken spheres at the bottom of the vial, we use a pipette to grab the bubbles at the top of the solution. Most of the times, these spheres have larger radii. These bubbles are placed in a Pyrex Petri dish to dry.

Once dried, we select the bubbles according to their sphericity and radii. Since the AFM's sensitivity is proportional to the radius of the sphere on the cantilever, using an optical microscope with an ocular with a calibrated scale, the bubbles with the largest radii are selected. To avoid systematic errors in the measurements, from that collection of bubbles, we choose the ones with a constant radius throughout them, making them now, mostly spherical. The manipulation and selection process is done with an optical fiber without buffer.

The effectiveness of this process is not without problems. However, it can remove most of the debris and we have been able to find spheres of around 100μm radius. While the latter is not always the case, this process, on average, seems to have increased the radii of the spheres we use for the experiments.

5.3.3 Assembly of the Modified Cantilever.

The rest of the fabrication of the cantilever is done mostly under an optical microscope using a mixture of commercial and homemade tools for manipulating the spheres and the cantilevers. Once the spheres are ready, as mentioned earlier, the prepared cantilevers are cleaned and etched again. Using a buffer-less optical fiber and under a 10X optical microscope, we grab a sphere from the Petri dish. The chosen sphere needs to have a large diameter, a smooth surface, and has to be free of debris. To attach it to the cantilever we use a dot of Silver Ag epoxy at the bottom of the free-end of the cantilever where the tip of the cantilever would be. The cantilevers we use are nevertheless tipless. The amount of epoxy has to be a small as possible because the resonant frequency of the cantilever will be higher.

The subsequent step is to thermally evaporate Au on the sphere and at the top of the free end of the cantilever. The Au on the top of the cantilever has to be evaporated only at the tip, about 50μm from the free end. The Au coating on the sphere and cantilever is about 100nm thick. To coat exclusively the mentioned parts, we use two razor blades to sandwich the chip that has the cantilever. Their sharp edges allow us to coat very selectively.

We use a homemade thermal evaporator that has a motor inside, rotating the razor setup and providing the sphere with a uniform Au coating. This instrument is equipped with a scroll pump and a turbomolecular pump that permits us to coat at about 10E-6 Torr. To avoid a rough Au surface, the coating has to be performed slowly and at large distances between the evaporator's boat and the cantilever; it takes about two hours, 3" of

gold wire, at a boat-cantilever distance of about 2.5” to achieve a uniform 100µm thick layer. To obtain these parameters, we correlated a smooth Au coating with the pressure buildup of the evaporator resulting from the coating process. This correlation has allowed us to obtain systematically smooth Au coatings, as has been demonstrated with roughness and thickness studies on the coatings and carried out with a commercial AFM.

After the coating process, we inspect the sphere and the cantilever with a 50X and a 100X objectives of an optical microscope. We reject cantilevers with spheres that have debris on sensitive areas of their surfaces, such as where the Au-coated spheres would contact the Au plate. (For a sphere of R ~ 50µm, the effective area is about 15µm X 15µm). Cantilevers having visible surface roughness on their spheres are rejected as well. In addition, since large coated portions of the cantilevers will decrease its quality factor, thus reducing microscope’s sensitivity, we reject cantilevers with more than 100µm long coatings on their top side. However, since small-coated portions of the cantilever will reduce the reflectivity of the interferometric cavity, we reject them when the top side coating is less than 25µm long. Irregular coatings and coated debris produce laser scattering, decreasing the amount of light in the interferometer cavity, modified cantilever with these characteristics are generally not chosen to be part of the experiment. In contrast, good quality modified cantilevers are kept in high vacuum while they are not in use, while the modified cantilever chosen for the experiment is prepared for its next stage. After the experimental measurements, the surface roughness of its sphere will be inspected with a commercial AFM.

5.4 Preparation of the Substrate.

We use a 12.7 mm Sapphire windows as substrate for the Au coating [101]. We chose this material for its surface quality, its hardness, its high thermal conductivity, and its chemical resistance. Its roughness is ~ 0.5 nm, as checked with a commercial AFM. This is an important starting point for Casimir force measurements. Its chemical resistance is useful because it can be cleaned of all debris, coated metals or organic materials. However when new, the windows are sonicated in a solution of hot DDW water with Liquinox for 15 min, then they are rinsed and sonicated with DDW until the detergent has been completely removed. The next step is to sonicate them in hot acetone and after that in hot IPA. To activate the surface we place the windows close to a UV lamp[] for 30 min. After which we insert the windows in the thermal evaporator for Au coating. The procedure to coat the windows is the same as the one for the cantilevers. In this case, however, we do not rotate the sample; only one side of the window is coated. When ready and before placing the coated window into the AFM, we often put the Au coated window in the UV lamp system for about 4 hrs. This recipe has produced satisfactory Au coatings. The effect of the UV exposure of the Au coating or its effect on the Casimir force measurements has not been thoroughly tested.

When the modified cantilever is prepared and assembled, as mentioned above, it is set on the Mo chip holder and aligned with the optical fiber. The Au coated window is placed on the Vespel fixture of the piezoelectric tube and the AFM is assembled. Before closing the AFM's can, we solder a thin magnet wire to the Au substrate with pure Indium solder. Low melting point, good adhesion with Au, and lack of flux are some of

the features of this solder. This choice makes the soldering procedure clean and quick, in contrast to the more messy and lengthy processes that use Ag epoxy.

5.5 Detection system.

We detect the cantilever and Au substrate displacements with two all-fiber Rugar type interferometers [18]. These custom-built interferometers consist of a laser diode pigtail with a 635 nm wavelength, various types of fiber couplers and two photodiodes. One photodiode detects the interferometric signal and the other one measures the laser power. Since all junctions between the components of the interferometer are spliced, stray interference and retroreflection to the laser diodes are minimized. In addition, to minimize laser and wavelength fluctuations we control the temperature and the power of the laser diodes. Figure 5.2 has a schematic diagram of an all-fiber interferometer coupled to the force microscope. Specifically for the interferometer made by the cantilever, the interferometric signal is analyzed with a Spectrum analyzer [90] while all the other photodetectors are connected to digital multimeters (DMM), including those used for the substrate interferometer. The advantage of this detection system, for both interferometers, is that only one leg of the fiber coupler needs to be introduced into the vacuum chamber; the rest of the components of the interferometer are outside the chamber and on an optical table. Due to large temperature variations in the laboratory, we have enclosed the optical table with 1.5” insulation board, maintaining the temperature variations of the table to less than half a degree. This allows us to use the optical table as a heat sink for the thermoelectrical coolers of the laser diodes and keeps most of the

interferometer components at a relative constant temperature.

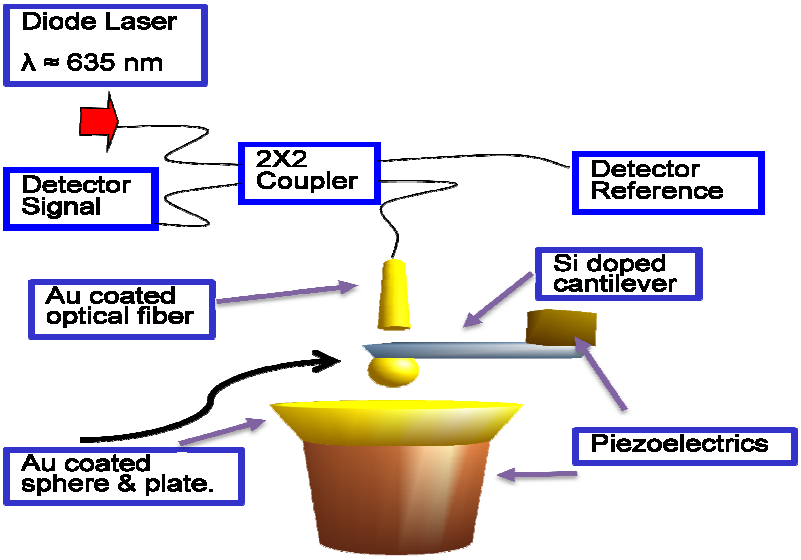

Figure 5.2. Schematic diagram of the all-fiber interferometer and the force microscope.

5.6 Vibration Isolation.

We isolate the microscope from external sources of vibration in two ways: Minimizing the mechanical coupling between the Dewar and two noisy sources, the vacuum pumps' system and the building vibrations, and reducing this same coupling between the Dewar and the microscope. Additionally, to shorten the effect of vibrational transients and reduce the amplitude of the AFM's oscillations, these two ways are equipped with damping mechanisms. We achieve the first task supporting the Dewar with a four-legged base consisting of a vibration-damping pad and a thick wood board. This setup is housed in a concrete pit in the basement of the Physics department. To reduce the coupling between the Dewar and the vacuum pumps' system we use a wooden sand box with lead bricks on top of the sand. Moreover, the vacuum line connecting the sand box

and the insert is held to the building floor with lead-shot sand bags. Since the insert is attached to the Dewar, to minimize the mechanical coupling between them, we place the microscope on the bottom stage of a two-stage springs system connected to the insert. The oscillations of the bottom stage are damped with a collection of Neodymium magnets. This magnetically damped system reduces the mechanical vibrations from exterior sources. In addition, the two-stage springs have been proven to be a better option for decoupling the bottom stage from the exterior vibrations than the single stage counterpart [102]. In Figure 5.1 we show the two-stage spring system and its final setup with the AFM. Note that while we have reduced the effect of exterior noise sources and damped the AFM's oscillations, the system still resonates. The calculated horizontal resonant frequency of the insert at the bottom stage is about 2 Hz. The calculated value of the vertical resonant frequency at the bottom stage is also about 2 Hz.

5.7 Vacuum system.

The experiments are performed in a vacuum of < 10e-4 Torr at room temperature and around 10e-6 Torr at T = 77 K and T = 6.3K. To achieve this, the main vacuum line consists of an oil-free vacuum system and a long line of bellows. The vacuum system combines a scroll pump and a turbomolecular pump that is connected to the insert trough the bellows. A gate valve separates the vacuum line from the insert. The insert has a stainless steel pipe that runs from the top of the Dewar to the lid of the can that contains the microscope. At the top of the insert there is a linear and rotary motion feedthrough connected to a manipulator that allows us to twist the head of the screw that changes

coarsely the separation distance between the sphere and the substrate. Note that the experiments are performed while the manipulator is retracted and not in contact with the two-set stage springs system.

To measure the pressure we use two thermocouple gauges located along the vacuum line. One measures the pressure main vacuum line and the other one the pressure of the insert. At room temperature the system pressure is < 10e-4 Torr.

At 77K and at 6.3K the main vacuum line gauge attains its minimum possible value ~10e-4 Torr but the gauge of the insert sets at ~10e-2 Torr. The value recorded by this gauge is incorrect because thermocouple gauges depend on the gas temperature. This gauge has not been properly calibrated to work at the gas temperatures at which we use it. To confirm this assumption we have performed He leak tests at room temperature and leak rate tests when the insert valve is closed and the temperature of the system is 300K and 77K. Considering the volume of our system, the results have been satisfactory for a system in high vacuum. One more verification of our assumption comes from the Q value of the modified cantilever in the microscope. That is, once the system has attained the base vacuum level the Q value at 77K does not present a substantial difference from the value at 300K. At 6.3K, this same verification is not possible because the temperature dependence of Q has a drastic effect [103]. Another argument in favor of our assumption is that the pressure inside the can at 77K and 6K should be lower than the one at room temperature since the can walls and the insert's pipe act as a cryopump during the cooldown of the system.

5.8 Cryogenics.

We use a 100 liters single-jacket Dewar to cool the insert to 77K and 6.3K. The insert is made mainly of Stainless Steel (SS) type 304. The reason is that it has low thermal conductivity and a high mechanical strength. This choice of material then reduces the transfer of heat from the top of the Dewar to the lid of the can. To avoid loosing mechanical strength, the can is made of the same material. Since it has low thermal conductivity, the walls and bottom of the can are very thin. While thermal radiation from the walls and can is not the main mechanism of heat transfer in our experiment, this is the most appropriate solution when, as in our case, no exchange gas is used during liquid Helium (LHe) cooldowns. To reduce thermal radiation and any heat flow between the top of the insert and the can, the insert has four Copper radiation baffles in different locations throughout the SS pipe of the insert. The lowest placed baffle is below the 77 K region or the Dewar's "belly". To minimize the laminar flow of the cryogenic fluid inside the Dewar we fit the baffles to the Dewar bore and we attached smaller copper disks to the baffles that fit the rest of the tubing of the insert. These baffles reduce the heat transfer by a factor of five and maintain an effective temperature gradient along the insert [96]. In our experiment, the dominant mechanism for transferring energy is thermal conduction. To enhance the thermal transfer from the lid to the stage where the AFM is located, we use a large piece of Copper for the first stage of the two-stage spring system. This Cu stage acts as a heat sink and allows a faster heat transfer to and from the microscope stage.

For the electrical wiring of the microscope, we use bundles of twisted-pairs of magnet

wire that are placed from the top of the insert to the lid of the can. At the top, they are connected to two connectors, a D-sub connector and a low-temperature 8-pin connector. At the lid, the wires are introduced to the can with a homemade feedthrough, a fixture that is made of Bronze and Stycast 2850-FT epoxy seal [96]. The Bronze fittings have an Indium (In) O-ring to seal them to the SS can. Magnet wire is also used inside the can for the electrical connections of the AFM. For these connections, to avoid the solder flux, we mostly used pure In solder.

Little was done to thermally anchor the electrical wires but some consideration was put in certain places where a lot of wire remained. Nevertheless, they are mostly attached to the metal tubing of the insert. Another reason this is not an issue is that the cooling power of the Dewar is high in comparison to the heat conducted through the magnet wires. In addition, the temperatures attained in this experiment are high for the heat from the wires to be a concern.

The optical fiber wiring is very similar to its electrical counterpart. Four optical fibers are held at the top of the insert with a plastic plug and weave through the insert. To introduce the fibers to the can, we use the same feedthrough that was described above. Except that it is thinner because there are fewer fibers than wires and the epoxy seal is less likely to leak.

5.8.1 Temperature Monitoring System.

We measure the temperature of the microscope using a Carbon-glass resistance temperature detector. To avoid temperature inaccuracies, we measure the resistance of the sensor with the four-probe technique. It has a temperature range from 1 K to 350 K and a

resolution of about 0.5 K.

This sensor is located under the lip that protrudes from the head of the microscope and is thermally anchored with GE Varnish. This location does not permit the entire sensor to have physical contact with the head. This means that the 6.3K reading might not be accurate. Another explanation is that the heat load on the instrument is too large and the equilibrium temperature is 6.3K. Since the temperature reading of the sensor is about 77.3K when the instrument is in a LN bath, we believe the second explanation is more likely. However, future versions of the temperature system will locate the sensor in a hole on the AFM head.

5.8.2 Instrument Low Temperature Specifications and Cooling Efficiency.

5.8.2.1 Room temperature to LN temperatures.

Starting from room temperature, the microscope takes two liquid Nitrogen (LN) transfers to keep the system at 77 K for two and a half weeks. The first one is to cool the system and the second one to keep it at LN temperature for a long period. Since there is no LN level on the system, we always fill the Dewar to the top. In about two days, the system reaches 77 K. It is then stable and ready for measurements. This process, while not the most efficient, has a boil-off rate that is satisfactory for our measurements at a base temperature about 77K. In addition, it allows us to make several measurement runs because our measurements take about 72 hours.

5.8.2.2 Room temperature to LHe temperatures.

To cool down the instrument we follow standard procedures with a single-jacket

Dewar. Richardson et al. [] have described this process in detail. The purpose of this process is two-fold: Cool down the instrument to LHe temperatures and waste the least amount of LHe in the process. LHe is an expensive, non-renewable commodity. This not being an unusual procedure the process is briefly recounted below. Particularities of the process are nevertheless highlighted.

To save LHe it is always best to precool with LN. In our experiment, before making measurements at LHe temperatures, we always measure the Casmir force at LN temperatures. This means the instrument is always precooled. However, after the LN measurements we transfer LN to the Dewar to cool most of the insert. When cold, to purge the LN from the Dewar, it is pressurized with Nitrogen gas (N_2). It is recommended to use a vacuum pump to remove the N_2 gas from the Dewar, as any Nitrogen residue, in any phase, can freeze. Our instrument does not permit us to perform this step. The Dewar then is filled with Helium gas (He) and after that we start the transferring of LHe to the Dewar.

From LN temperatures, the instrument needs about 60 liters to cool down and 60 liters to remain at its base temperature for about a week. Ideally, this allows us to carry out two measurement runs. Until now, we have achieved only one measurement run. To maintain the temperature a base temperature of about 6.3K for one more week, one transfer of 60 liters of LHe is enough.

5.9 Automisation.

Using the software LabView, we made various programs that control most of the

functions of the microscope. Two of them control and monitor the microscope's actions while it is running. On of these programs is called Main.Vi. It collects the response of the cantilever to the thermal noise from a Spectrum analyzer through a GPIB interface. It sets the voltages applied between the modified cantilever and the Au substrate through a low-noise voltage supply. Using a similar voltage source, this program controls the voltage applied to the piezoelectric tube that regulates the separation distance between the Au substrate and the sphere. In summary, when Main.Vi is running, it measures the response of the cantilever at different voltages between the sphere and the substrate for many different voltages applied to the piezoelectric tube

The second program called CryoTemp.Vi controls the temperature and monitors the power of the laser diode corresponding to the cantilever interferometer. It also monitors the relative displacement of the Au substrate with respect to the optical fiber end. We use this signal to calibrate the displacements of the piezoelectric tube. In addition, this program monitors the temperature of the microscope, the temperature, and the power of the laser diode that corresponds to the interferometer of the substrate. The software records most of the input and output data of the system for subsequent data analysis.

5.10 Grounding.

It is important to avoid or minimize grounding problems of the system. Ground loops are the most common problem disturbing our detectors. However, non-ohmic contacts or loose contacts in any part of the microscope can also modify the electrostatic voltages between the components of the microscope. For this reason, the instruments must have

good solid soldering junctions. To address the ground loop problems, we choose the body of the microscope to be our main and only ground, which is, at the same time, the ground from the laboratory. The microscope's body is connected to the laboratory ground through the plumbing of the vacuum pump system. All electronic instruments used in the experiment are connected to the same lab ground. In addition, all the ground wires come from the ground of the microscope and are not connected at any point in between. Nevertheless, if the Au-coated sphere does not have the same potential as the body of the microscope, the electrostatic force is not going to be compensated properly and the Casimir measurements will not be accurate. As can be seen in the “fabrication of the modified cantilever” section, a great effort has been put into making sure this scenario is unlikely in our experiment. In conclusion, we have found that when the modified cantilever has minimal electrical resistance between its components, and all the electrical instruments used in the apparatus are grounded through the microscope, then the ground loops are minimized and the amount of bad contacts reduced.

5.11 System procedures.

Other than experiments like Iannuzzi et al. [82], most of the procedures to measure the Casimir force are similar. All of them measure a force or the gradient of a force between a sphere and a plate. The resultant force, or its gradient, is due to the Casmir force and the electrostatic force between these objects. For Casmir force experiments, researchers modified the latter force to find the contact potential (V_0), which is the residual potential when plate and sphere are at the same electric potential. For this

purpose, they set different voltages between the sphere and the plate. Since the electrostatic force depends quadratically on the voltage between the sphere and the plate, the measured force or gradient will have a parabolic dependence with respect to those voltages. Since the experimenters' objective is to explore solely the Casmir effect, they aim to measure the force when the electrostatic force is between near compensation to when its strength is comparable to the Casmir force. This means that the voltages between the sphere and the plate are set to be around V_0. Experimentally, these values are less than a volt away from V_0. Furthermore, these voltages produce a parabola with an apex at V_0 and the value of the Casmir force (force gradient). The curvature of the parabola is proportional to the strength of the electrostatic force (force gradient). Note that this parabola corresponds to a certain distance between the sphere and the plate. For other distances, the result is the Casmir force (force gradient) as a function of distance. Experimentally, however, the absolute distance between the sphere and the plate is not known precisely; only the relative changes in distance are known precisely. To find the absolute distance researchers use the curvatures of the parabolas at different distances. Since, as we mentioned above, they are proportional to the distance dependence of the electrostatic force. In combination with the relative distance changes, the curvature is used to find the absolute sphere-plane distance. Specifically researchers look for the average plate-sphere contact or smallest distance or z_0, which when added to the relative distance changes yields the distance between the sphere and the plate. Different methods are used to obtain z_0. Once obtained, however; researchers can obtain the Casmir force (force gradient) as a function of distance between a sphere and a plate. Note z0 is a

precise value because the theoretical electrostatic force between a metallic sphere and metallic plate is an exact expression.

Our procedure is very similar to the one described above. Since it is a dynamic measurement, we measure the gradient of the force between a sphere and a plate. Essentially, we measure a resonant frequency of the modified cantilever at infinity, which is when no force is exerted on the sphere. After that, we measure the same frequency at distance where there is a force exerted on the sphere. We repeat this for several distances. The differences between each of these frequencies and the resonant frequency at infinity, in combination with the curvatures of their corresponding parabolas, result in the Casmir force gradient as a function of the separation between a sphere and a plate. This function and Eq. XX of chapter 2 yield the Casimir pressure as a function of distance between two plates.

The experimental steps we follow to measure the Casimir pressure are the following:

I. At a separation distance larger than 300 micron: We measure the resonance peak of the modified cantilever at infinity using the program Main.Vi while monitoring the status of the instrument with the program CryoTemp.Vi. To reduce random noise, the spectrum analyzer averages ten peaks at a resolution of 30.5 mHz and Main.Vi records the averaged peak. The average peak is measured around 100 times for statistical purposes. The software running the experiments is stopped and data is analyzed. The resonant frequency of the modified cantilever is the averaged value obtained from the 100 peaks. The standard error is also obtained from this average.

II. When step one is finished and without modifying the separation between the sphere and the plate. We applied a voltage of 200 mV between the sphere and the plate. We proceed to coarsely approach the sphere to the sample. To be able to separate the sample from the sphere when in contact, we reduce the sample-plate distance by 1 micron. During the coarse approach the sphere will contact the substrate, pulling the substrate away with a 500 nm step might help separate them. Using the coarse linear manipulator we twist the screw of the microscope to approach the sphere to the plate. This process is time consuming because slow approaches avoid the sphere crashing on the substrate or being compacted between the plate and the optical fiber end that forms the interferometric cavity. Both problems result in the cantilever being destroyed.

III. Once the electrostatic force gradient is detected, the resonant frequency of the cantilever is smaller, the manipulator is retracted and a rough estimate of the separation distance is calculated. That value helps us to approach the sphere toward the plate in an efficient manner. V_0 is roughly measured by manually setting different voltages between the sphere and the plate and observing the resonance peak shift frequencies.

RETRACTING THE LINEAR MANIPULATOR

Since the electrostatic force has been detected, the sphere-plate distance is less than two μm. This means that a slight nudge on the instrument makes the sphere contact the plate or on the contrary, makes it move too far from the sample to

detect a force using the plate's fine approach. For this reason, to retract the manipulator and still detect a force requires us to gently rotate the manipulator counterclockwise so its tip stops touching the sides of the groove on the microscope's screw. Since the groove is quite small, the rotation has to be minimal. Once this is achieved, the manipulator has to be slid as gently as possible for about five inches. This stops the manipulator from contacting the two-stage spring system. Furthermore, the manipulator is held with a Cajon-type connector, tightening this fixture has to be equally gentle. If after this process, the cantilever still detects a force the experiment can continue. If not, the manipulator has to be gently set on the screw of the microscope and the sphere-plate approach started once more i.e. go back to step two.

IV. Measuring V_0: We measure the resonance peak of the modified cantilever using the program Main.Vi. by obtaining a averaging 10 peaks with a resolution of 121 mHz on the spectrum analyzer . Main.Vi records it. This is performed at each of the nine voltages roughly used in step three. Note that the average peak has 10 peaks averaged linearly and without overlap. This means that peak's data are averaged arithmetically and that each peak's data is independent from one another.

V. Step 4 is repeated at different separation distances to roughly check the dependence of V_0 with separation distance. To save time this is typically performed at a lower resolution than in the experiment: 121 mHz. If the V_0 changes substantially with distance, we might replace the Au substrate, replace

the modified cantilever, replace both, or change point of sphere-plate contact. The circumstances of the experiment will lead us to decide the most appropriate option. In the case where V_0 is relatively constant, we will continue the experiment. Before starting the experiment, we let the piezoelectric tube equilibrate as no precautions to minimize the drift were taken when the voltage was applied to it. This might take from a couple of hours to half a day. We monitor the status of the piezoelectric tube with the program CryoTemp.Vi.

VI. Start of the experiment: The Main.Vi program performs step four at different separation distances. The distance step between measurements and the initial estimated absolute distance between the sphere and the plate are set in the program. In addition, we set the time between steps. We use this to minimize the piezoelectric tube drift, as the chosen time is larger than its characteristic relaxation time for the distance steps being used in the experiment. The resolution of 30.5 mHz is also set in the program. During these measurements, the program CryoTemp.Vi will monitor the status of the experiment.

VII. During the experiment, we modify the distance step between measurements and the voltages applied to the substrate. The shorter the separation distances the smaller the distance step. Note that the Main.Vi program has to be stopped to change the distance step and has to be restarted with the new distance step. The voltages applied between the sphere and the plates are chosen so the maximum frequency shift is 4 Hz. This stops the peaks from moving away from the scope of

the Spectrum analyzer. When the sphere is close to contact the plate, the frequency range of the Spectrum analyzer has to be shifted constantly to allow the peaks to be inside that frequency range.

VIII. Once the resonance peak disappears or the Q changes substantially we stop the experiment. This means that we stop both programs. The sphere might have touched or is about to touch the plate. We retract the plate with the piezoelectric tube and, if needed, repeat the experiment when the piezoelectric tube equilibrates.

IX. After all experiments are finished the resonance frequency at infinity is measured as in step 1. Substantial changes in frequency between the average value in this step and the value in step 1 could mean that the sphere picked up or lost mass while in contact with the plate. To perform this step the linear manipulator has to be lowered and touch the screw of the microscope. This critical procedure, if performed carelessly, can lead to breaking the cantilever. This is because the sphere and the plate are at most two μm apart. If the manipulator is not lowered slowly or gently put on top of the screw, the cantilever or sphere might break. The same care should be observed when rotating the screw to separate the sphere from the plate. The rotation has to be in small steps, at least for one whole turn.

X. Au-coated sphere and Au-coated plate are retrieved from the microscope to measure their surface roughness and their electrical conductivity.

6 Results and Discussion

In this chapter, the main results of the experimental study of this manuscript are presented. The chapter is divided into three sections. In the first section, we present the experimental values of the Casmir pressure between two plates at T = 6.7 K. In sections

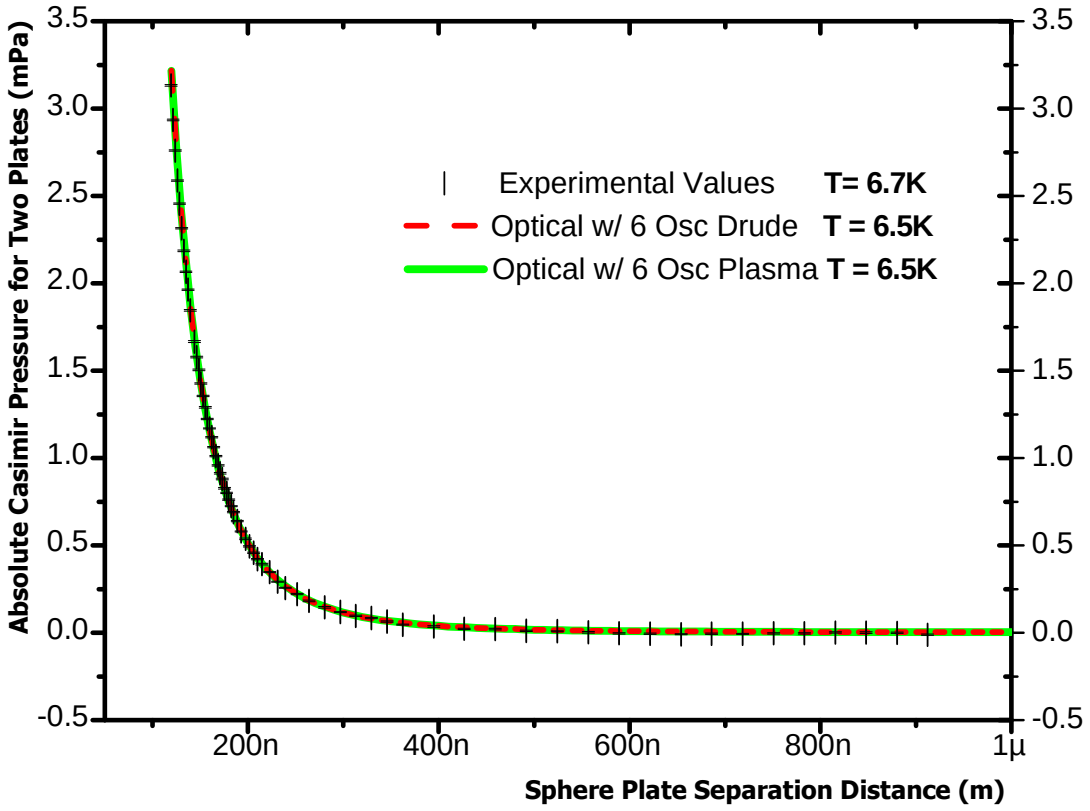

Figure 6.1. Experimental and theoretical values for the magnitude of the Casmir pressure between two plates as a function of the sphere-plate separation distance at T = 6.7 K. The black crosses are the experimental values with their corresponding error bars at T = 6.7 K. The red dashed line is the pressure calculated with the generalized Drude-like model with six transitions of the core electrons at T = 6.5 K. The green solid line is the Casmir pressure calculated with the generalized Plasma-like model at T = 6.5 K with six transitions of the core electrons.

two and three the corresponding values for T = 77 K, and T = 300 K are presented. These results are compared to the theoretical values of the Casmir pressure calculated using the generalized Plasma-like and Drude-like models at these three temperatures.

6.1 Casimir force between two Au plates at T = 6.7 K

At this temperature, the experimental values for the Casmir pressure had the best agreement with the corresponding theoretical values calculated for the different models. The reason seems to be that the systematic errors in the experimental setup are minimized at this temperature. While this allowed to precisely measuring the Casmir pressure between two plates from 120 to 600 nm, the measurements were performed at distances up to 900nm. The baseline produced by the Casmir pressure measurements from 600 nm to 900 nm is needed to calibrate the sphere-plate separation distance. The dominant contribution in this distance interval is the electrostatic force between the sphere and the plate, which is used to obtain their absolute separation. Using this method, at this temperature, it resulted in a minimum separation between the sphere and the plate of $z_0^* = 119.4\,\mathrm{nm}$. Using this value, measured values of the Casmir pressure are compared with the theoretical values as a function of the separation distance. . They are presented in fig. 6.1 as black crosses. . In addition to the experimental values, this figure contains the calculated Casmir pressure between two plates for two theoretical models of the plate material. The red dashed line represents the theoretical values using the generalized Drude-like model at T = 6.5 K and the green solid line represents the corresponding values for the generalized Plasma-like model at the same temperature. Both graphs are calculated using the process described in the subsection called:

Generalized Plasma-Like Model and Optical Tabulated Data and the Drude Model respectively. Specifically, these two curves are calculated using six transitions of the core electrons.

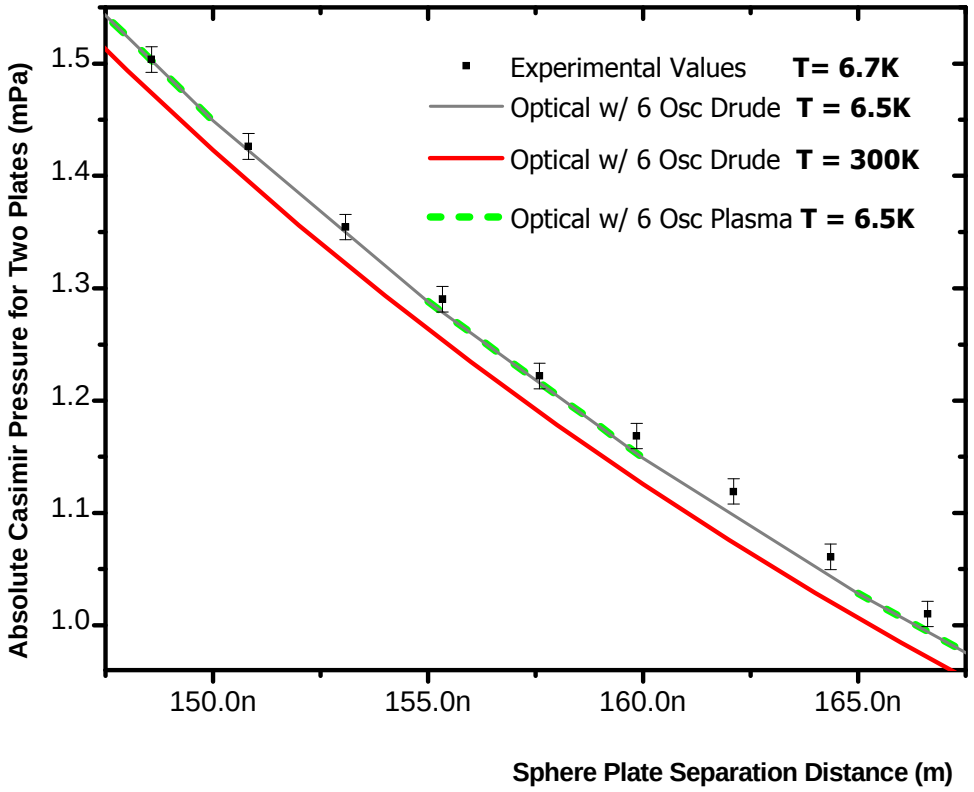

Figure 6.2. Experimental and theoretical values for the absolute Casmir pressure between two plates as a function of the sphere-plate separation distance. The black squares are the experimental values with their corresponding error bars at T = 6.7 K. The grey solid line is the pressure calculated with the generalized Drude-like model with six transitions of the core electrons at T = 6.5 K. The red solid line is the Casmir pressure calculated with the generalized Drude -like model at T = 6.5 K with six transitions of the core electrons. The green dashed line is the Casmir pressure calculated with the generalized Plasma -like model at T = 6.5 K with six transitions of the core electrons.

The results presented in this report are highly promising in the range of 150 nm to 230 nm. They have < 1 % relative random error and their degree of agreement with theoretical calculations at T = 6.7 K is < ±2 %. To appreciate graphically the

experimental precision of these results, in fig. 6.2 they are presented in the interval that ranges from 148 nm to 167 nm, in fig. 6.3, from 165 nm to 195 nm, and in fig. 6.4 from 195 nm to 230 nm. In addition, both graphs plot the calculated values of the Casmir pressure between two plates for T= 6.7 K (grey solid line) and for T = 300 K (red solid line) using the generalized Drude-like model, and for T = 6.5 K (green dash line) for the generalized Plasma-like model. Note that the corresponding theoretical values for the latter model at T = 300 K are not in the graphs of this chapter. They have a small temperature variation when compared to the values of the pressure calculated with the generalized Drude-like model approach at T = 300 K. Instead the latter is presented and compared with the experimental data at T = 6.7 K.

6.1.1 Experimental precision of the Casimir Pressure.

The relative random error per data point is calculated using the expression given by,

6.1

$$\delta P^{r}(z_i) = \frac{\Delta P(z_i)}{P_{exp}(z_i)}.$$

Where $P_{exp}(z_i)$ is the experimental value and $\Delta P(z_i)$ is the error obtained through propagation of the errors of the measured quantities i.e., the resonant frequency of the cantilever, V_0, and the curvature of the parabolas described in chapter 5. We use the following expression to calculate this value,

6.2

$$\Delta P(z_i) = \frac{1}{\pi}\left[\left(\frac{k}{Rf_0}\Delta f\right)^2 + \left(\frac{kf(z_i)}{Rf_0^2}\Delta f_0\right)^2 + \left(\frac{f(z_i)-f_0}{f_0}\left(\frac{k}{R}\right)^2 \Delta\left(\frac{R}{k}\right)\right)^2\right]^{1/2}.$$

Where R is the radius of the sphere, k the spring constant of the modified cantilever, and $f_0$is the resonant frequency of the modified cantilever when no force is exerted on the sphere (at infinite distance). In contrast, the f is the resonant frequency of this cantilever when the sphere is in a force gradient. Note that the dominant term in this expression is the first one on the right hand side and Δf proportional to the resolution set by the experimenters in the Spectrum analyzer.

The numerical values on the right hand side of eq. 6.2 for example, at T = 6.7 K, are found using the procedure in step 1 of chapter 5. This procedure then, yields a mean value of $f_0 = 3322.8345\,Hz$, a standard error of $\Delta f_0 = 4.6\,\text{mHz}$, and a standard deviation for a 10 average Lorentzian peak of $\Delta f = 67.3\,mHz$. The value *R/k* is obtained indirectly through electrostatic calibration.

A discussion of the contribution of the systematic errors to the experimental precision is found below. However, for the distance intervals in figs. 6.2-4, eq. 6.1 and eq. 6.2 obtain a relative random error for the experimental values of the Casmir pressure of less than 1 %.

6.1.2 Comparison between Theory and Experiment.

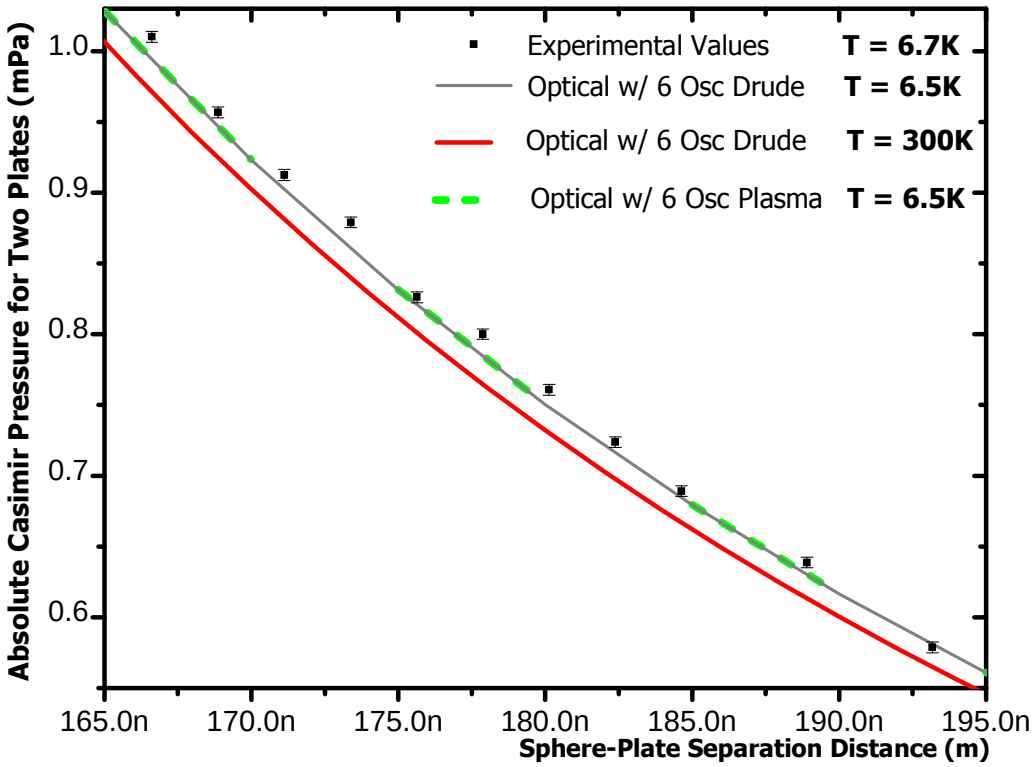

Figure 6.3. Experimental and theoretical values for the absolute Casmir pressure between two plates as a function of the sphere-plate separation distance. The black squares are the experimental values with their corresponding error bars at T = 6.7 K. The error bars are slightly bigger than the squares. The grey solid line is the pressure calculated with the generalized Drude-like model with six transitions of the core electrons at T = 6.5 K. The red solid line is the Casmir pressure calculated with the generalized Drude -like model at T = 6.5 K with six transitions of the core electrons. The green dash line is the Casmir pressure calculated with the generalized Plasma -like model at T = 6.5 K with six transitions of the core electrons.

Inspection of figs. 6.2-4 shows that the experimental values for T = 6.7 K have

good agreement with the calculated values of the Casmir pressure when using the generalized Drude-like model at T = 6.5 K $\left(P_{Drude6.5K}(z_i)\right)$. At this temperature, the latter values and the calculated pressures using the generalized Plasma-like model is

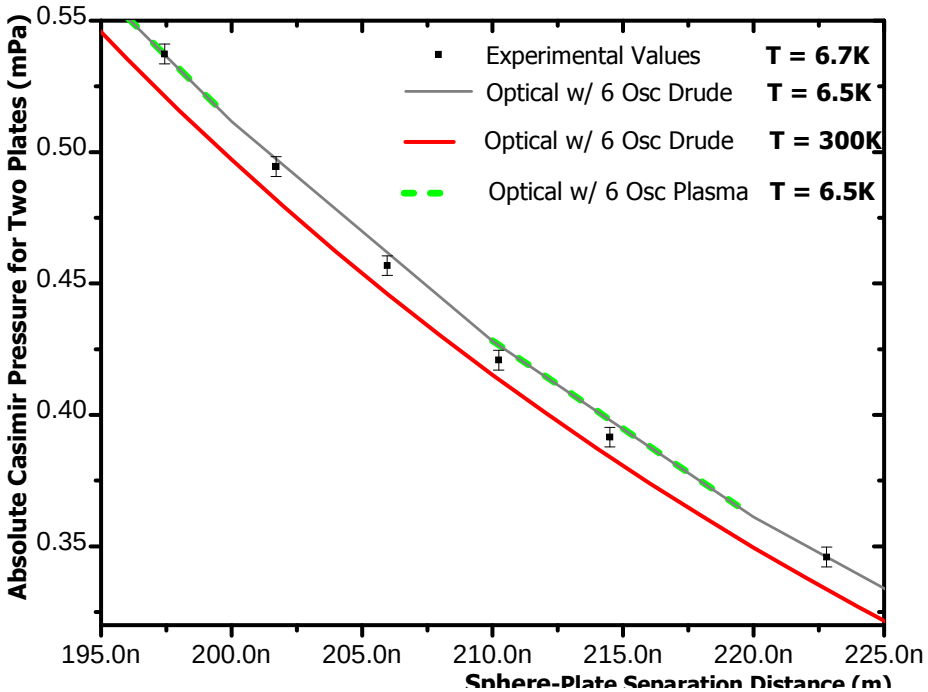

Figure 6.4. Experimental and theoretical values for the absolute Casmir pressure between two plates as a function of the sphere-plate separation distance. The black squares are the experimental values with their corresponding error bars at T = 6.7 K. The grey solid line is the pressure calculated with the generalized Drude-like model with six transitions of the core electrons at T = 6.5 K. The red solid line is the Casmir pressure calculated with the generalized Drude -like model at T = 6.5 K with six transitions of the core electrons. The green dash line is the Casmir pressure calculated with the generalized Plasma -like model at T = 6.5 K with six transitions of the core electrons.

larger than the sensitivity of the instrument used here. For reasons explained below, the experimental results $\left(P_{Exp6.7K}(z_i)\right)$ then are compared to $P_{Drude6.5K}(z_i)$ for the all z_i's. To achieve this, the following percent uncertainty approach is used:

6.3

$$\%\ percent\ uncertainity\ (z_i) = 100 \cdot \frac{P_{Drude6.5K}(z_i) - P_{Exp6.5K}(z_i)}{P_{Drude6.5K}(z_i)},$$

Using eq. 6.3, it is shown in fig. 6.5 that for the sphere-plate separations of fig.

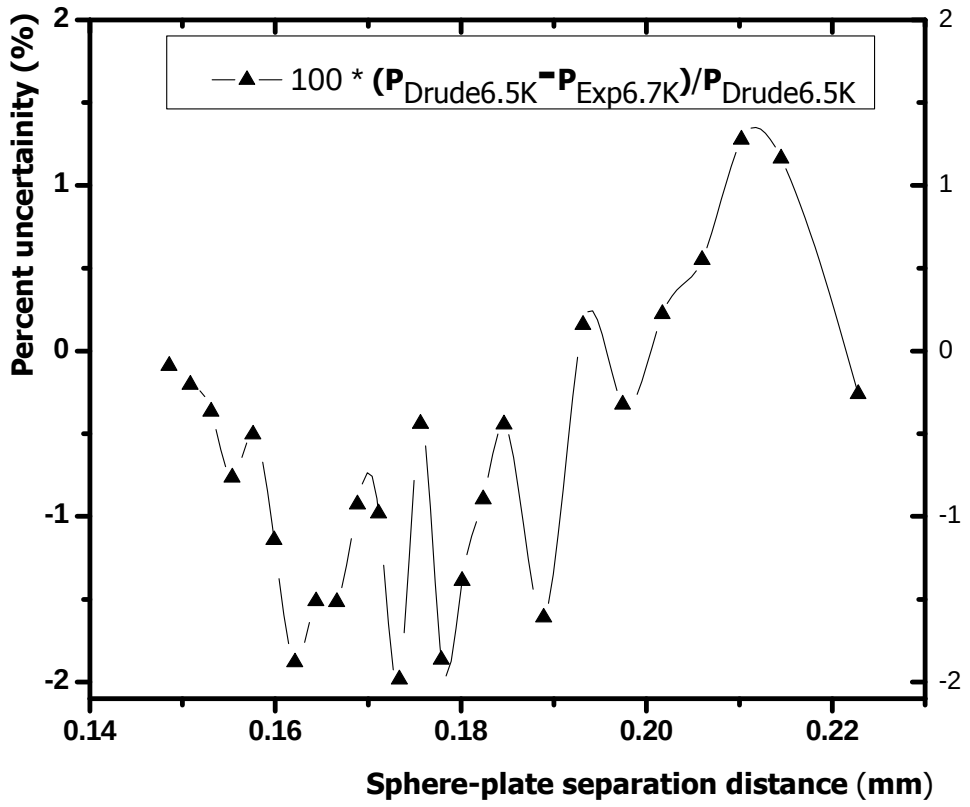

Figure 6.5. Degree of agreement between the pressure calculated with the generalized Drude-like model with six transitions of the core electrons at T = 6.5 K and the experimental measurements of the Casmir pressure at the same temperature.

6.2-4 the degree of agreement between experimental and calculated values is less than ±2 %. To obtain this quantity, the calculated values were interpolated between 120 nm and 1000 nm every 0.25 nm from values calculated every 5 nm. This allowed for the parameters of eq. 6.3 to be evaluated at effectively the same z_i.The same procedure is

used to show the degree of agreement between the Casmir pressure calculated at T = 300 K using the generalized Drude-like model $\left(P_{Drude300K}(z_i)\right)$ and $P_{Exp6.7K}(z_i)$ in the same distance range as fig. 6.5. In this case, the pressure values obtained through interpolation are calculated every 0.25 nm and in the same separation distance interval as above. However, the interpolation uses calculated data from separation distance that is separated by 2 nm. For this case, the percent uncertainty has an expression given by,

6.4

$$\%\, percent\ uncertainity\ (z_i) = 100 \cdot \frac{P_{Drude300K}(z_i) - P_{Exp6.5K}(z_i)}{P_{Drude300K}(z_i)},$$

Note that eq. 6.4 compares the calculated values at T = 300 K with the experimental values at T = 6.7 K. The results of this expression, as well as the ones from eq. 6.3, are plotted together in fig. 6.6 as a function of the sphere-plane separation distance. The red open circles curve is obtained with eq. 6.4 and the black open triangles curve with eq. 6.3. The advantage of both curves being in this figure is that a discrepancy between the experimental results at T = 6. 7 K and the calculated data at T= 300 K is emphasized. That is, the data from eq. 6.4 is a factor of about two bigger than the data from eq. 6.3. Therefore, if the experimental values of the Casmir force at T = 300 K are obtained and compared to the pressure at T = 300 K calculated with the generalized Drude-like model, the instrument used here could measure, for the first time, the thermal effects of the Casmir effect due to materials with non-zero dissipation. Otherwise, the experimental results at T = 300 K will be in much better agreement with the pressure calculated with the generalized Plasma-like model at T = 300 K. As it can be seen from

figs. 6.2-4 the thermal effects in the latter case are smaller than for the pressure calculated with the Drude-like model.

It is illustrative to compare some of the experimental values of the Casmir

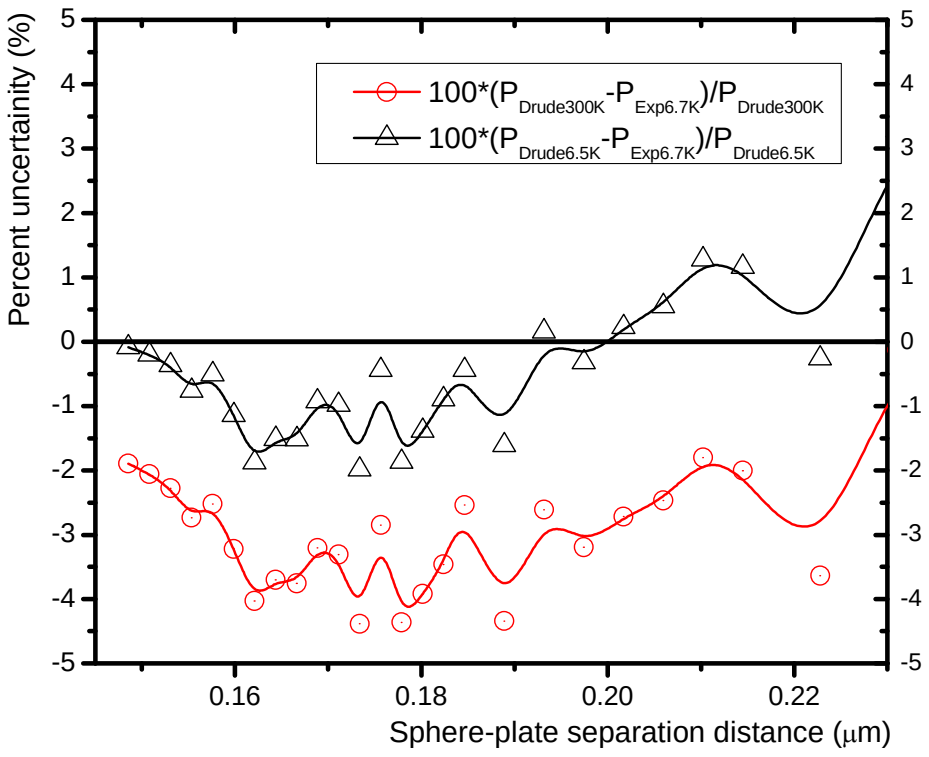

Figure 6.6. Comparison between the percent uncertainty at T = 6.5 K and T = 300 K. The values at 300 K result from the comparison between the pressure calculated with the generalized Drude-like model with six transitions of the core electrons at T = 300 K and the experimental measurements of the Casmir pressure at T = 6.5 K.

pressure at T = 6.7 K to the theoretical Casmir pressure between two plates calculated with the generalized Drude-like model at T = 77 K, as the thermal effects are more pronounced than in the corresponding Plasma-like model. For this purpose, in Figure 6.7 the experimental values at T = 6.7 K from 146 nm to 160 nm are presented. The figure also includes the corresponding theoretical values for the Casmir pressure between two

plates at T = 77 K. In addition, the theoretical curves presented in previous figures for the Casimir pressure at different temperatures and for different material's model are plotted as a reference. In Figure 6.7, the dark cyan solid line represents the theoretical values of

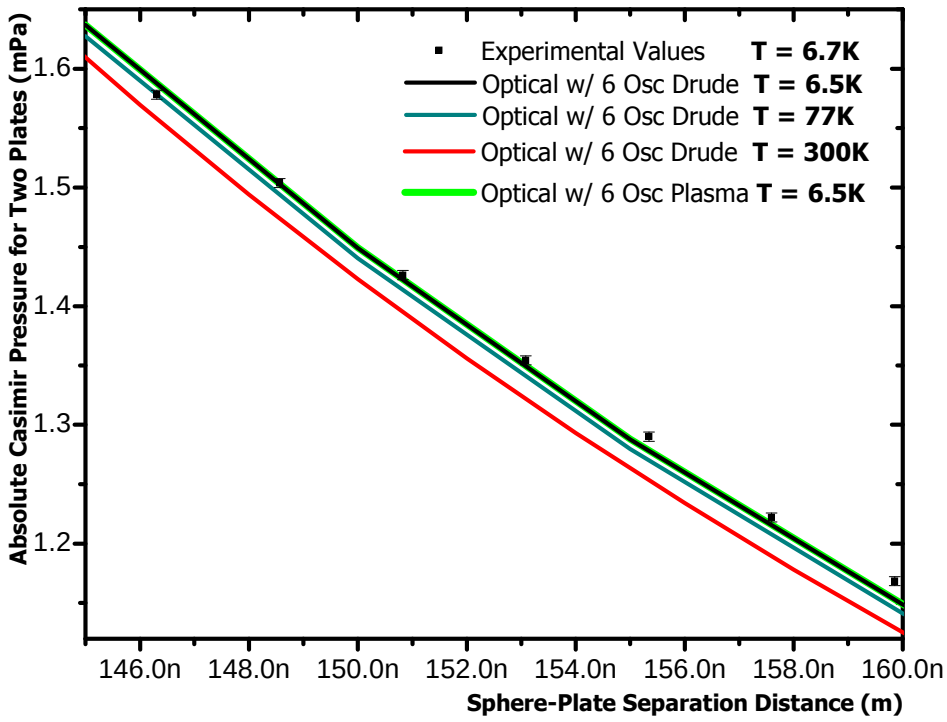

Figure 6.7. Experimental and theoretical values for the absolute Casmir pressure between two plates as a function of the sphere-plate separation distance and for different temperatures. The black squares are the experimental values with their corresponding error bars at T = 6.7 K. The error bars are slightly bigger than the squares. The black solid line is the pressure calculated with the generalized Drude-like model with six transitions of the core electrons at T = 6.5 K. The dark cyan solid line is the Casmir pressure between two plates calculated using the generalized Drude-like model and at T = 77 K. The red solid line is the Casmir pressure calculated with the generalized Drude -like model at T = 300 K with six transitions of the core electrons. The green solid line is the Casmir pressure calculated with the generalized Plasma-like model at T = 6.5 K with six transitions of the core electrons.

the pressure at T = 77K calculated with the optical tabulated data for Au in the generalized Drude-like model.

Figure 6.7 underscores the difference between the measurements at T = 6.7 K and the calculated values of the Casmir pressure at T = 77 K and T = 300 K when the generalized Drude-like model is used. The degree of agreement between $P_{Exp6.5K}(z_i)$ and the corresponding theoretical values at T = 77 K, $\left(P_{Drude77K}(z_i)\right)$, is on the 2% uncertainty range. Similar to the quantity found when comparing to $P_{Drude6.5K}(z_i)$. However, with the current sensitivity of the instrument that is used here, this figure demonstrates that thermal effects of the Casimir effect might be found when comparing $P_{Exp6.5K}(z_i)$ with $P_{Exp300K}(z_i)$ and not with $P_{Exp77K}(z_i)$. This will be more significant below, in the discussion of the systematic errors of the measurements. This is the case because the instrument used in this experimental study has lower systematic errors at T = 77 K than at T = 300 K. This makes the former temperature a preferred environment to perform this type of experiments.

The experimental values in this figure have a larger relative random error than the experimental values in figs. 6.2-4. Using eq. 6.1 and eq. 6.2, at about 230 nm the first value has 1.3 % relative random error, at about 345 nm it is 6 %, and at about 400 nm it has 11 %. To obtain a more precise experimental measurement, the error could be reduced by averaging different T = 6.7

K experiments, or increasing the number of averaged curves per experimental value of the Casmir pressure. This would reduce the statistical uncertainty of the resonant frequency of the cantilever. Inspection of eq. 6.2, however, shows that increasing the

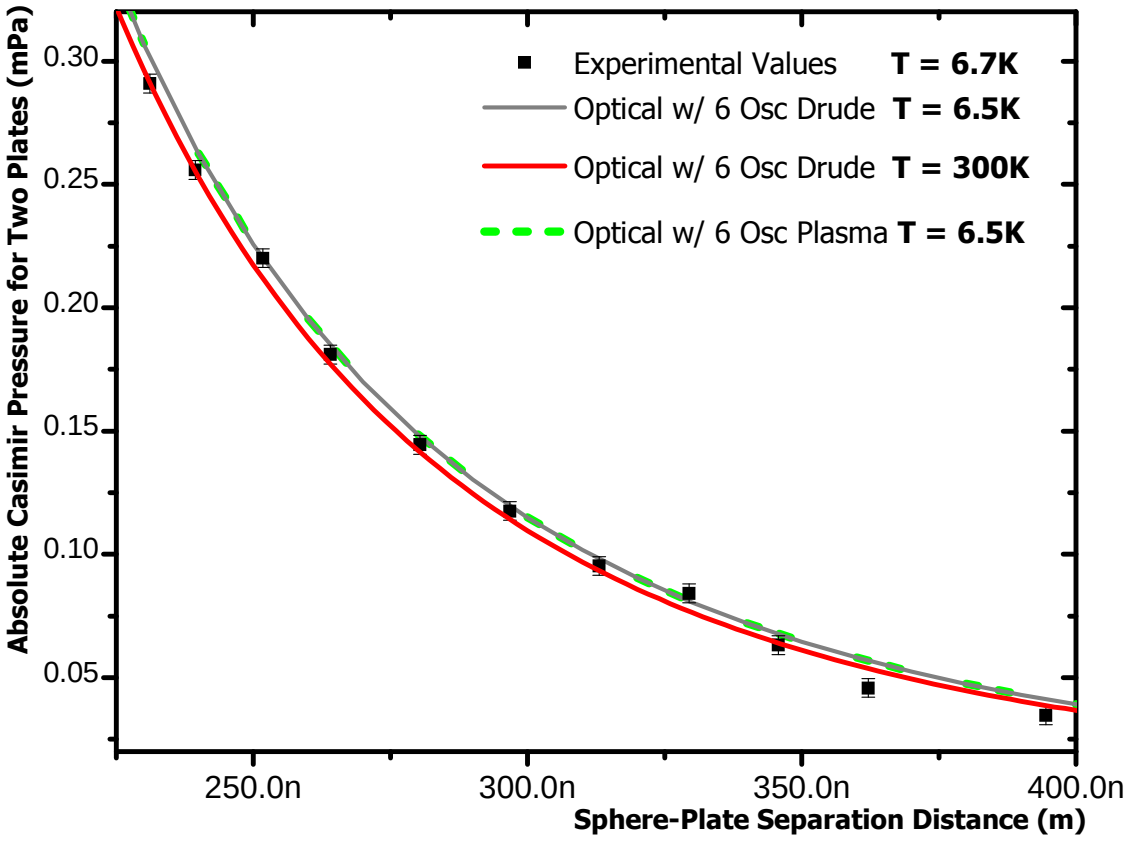

Figure 6.8. Experimental and theoretical values for the absolute Casmir pressure between two plates as a function of the sphere-plate separation distance. The black square are the experimental values with their corresponding error bars at T = 6.7 K. The grey solid line is the pressure calculated with the generalized Drude-like model with six transitions of the core electrons at T = 6.5 K. The red solid line is the Casmir pressure calculated with the generalized Drude -like model at T = 6.5 K with six transitions of the core electrons. The green dash line is the Casmir pressure calculated with the generalized Plasma -like model at T = 6.5 K with six transitions of the core electrons.

resolution at which the frequency is measured is more rewarding. Additionally, a combination of factors, such as reducing the modified cantilever spring constant k, increasing the radius of the sphere, and increasing the resonant frequency f_0 of the modified cantilever, can highly improve the pressure sensitivity of the microscope. This is one of the reasons the preparation of the modified cantilevers is vital in avoiding any increase of the k and reduction of the f_0. Hollow spheres for the modified cantilever should be preferred as a larger mass decreases f_0. To increase the measurement precision in this and other separation distance intervals, future experiments will be performed with higher sensitivity cantilevers. This type of cantilevers has been already studied by our group [104].

The degree of agreement between the experiment and the corresponding theory can be improved. Using the percent uncertainty expressions of eq. 6.3 and eq. 6.4, equivalent curves to Figure 6.6 was obtained in the separation distance interval of **Error!**

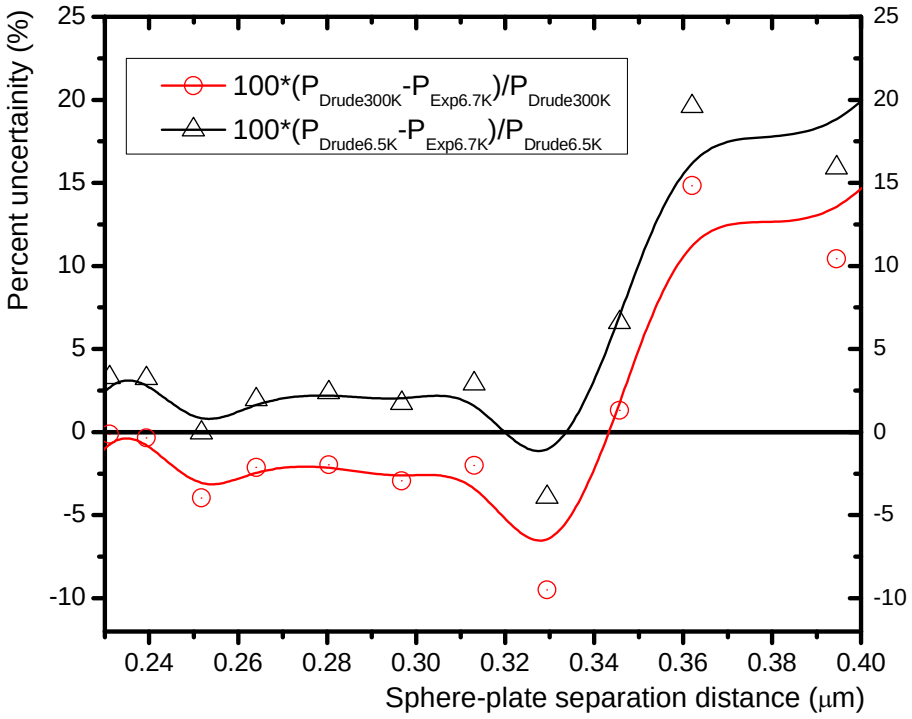

Figure 6.9. Comparison between the percent uncertainty at T = 6.5 K and T = 300 K. The values at 300 K result from the comparison between the pressure calculated with the generalized Drude-like model with six transitions of the core electrons at T = 300 K and the experimental measurements of the Casmir pressure at T = 6.5 K.

Reference source not found.Error! Reference source not found.. These curves are plotted in Figure 6.9. This figure shows that, while the experimental measurements have good agreement with the theory, about 5% up to 320 nm, they are not sensitive enough to resolve the temperature dependence of the Casmir pressure between plates.

Figure 6.10 present the experimental values of fig. 6.1 at separation distances that range from 400nm to 900 nm along with its theoretical curves and the curve for the Casmir pressure at T = 300 K calculated using the generalized Drude-like model. Using

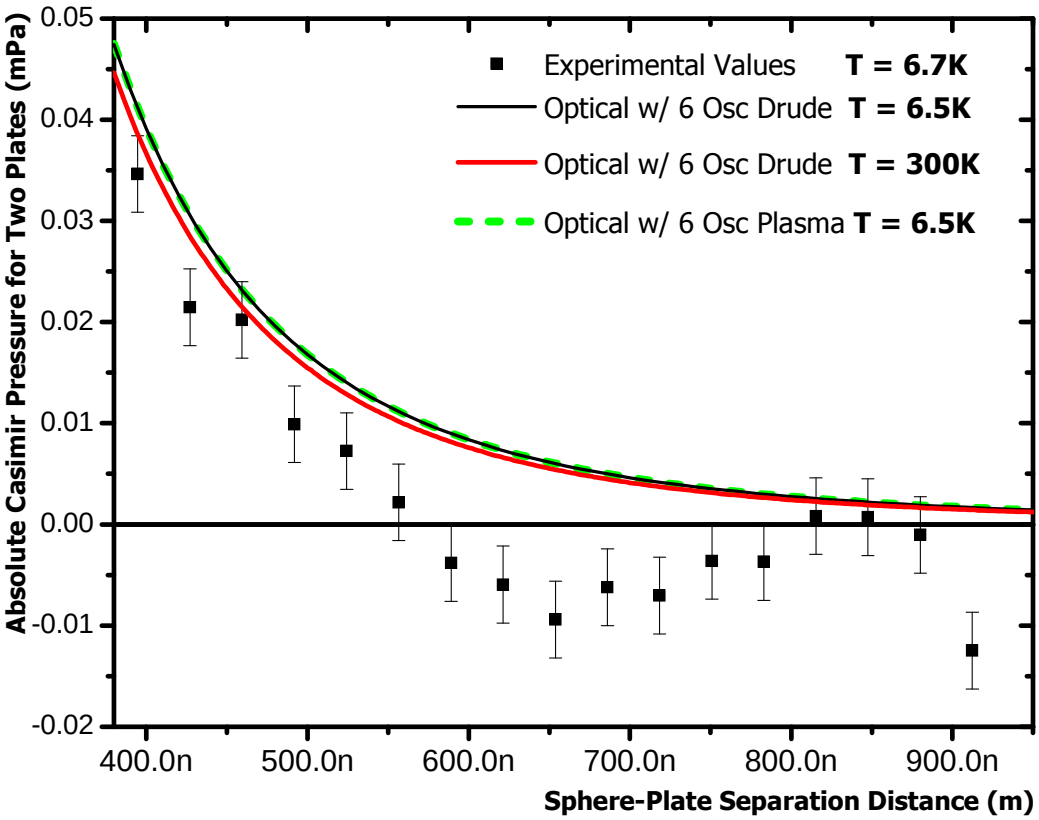

Figure 6.10. Experimental and theoretical values for the absolute Casmir pressure between two plates as a function of the sphere-plate separation distance. The black square are the experimental values with their corresponding error bars at T = 6.7 K. The grey solid line is the pressure calculated with the generalized Drude-like model with six transitions of the core electrons at T = 6.5 K. The red solid line is the Casmir pressure calculated with the generalized Drude -like model at T = 6.5 K with six transitions of the core electrons. The green dash line is the Casmir pressure calculated with the generalized Plasma -like model at T = 6.5 K with six transitions of the core electrons.

eq. 6.1 and eq. 6.2, it can be shown that the precision of the experimental data is lower than previous data. For example, at about 426 nm the relative percent error is 17.6 %, at

524.2 nm it is 52.2 % nm, and at higher separation distances it goes beyond a 100 %. Fig. 6.10, however, demonstrates the sensitivity of the instrument used here. It shows that the for separation distances larger than 524.2 nm the signal to noise ratio is less than 1. In addition, while revisiting the experimental values from fig. 6.10 it is found that for distances higher than 524.2 nm, where effectively the microscope does not detect any pressure, the random uncertainty of the experimental points is 5.3 μPa. This is about 39 % higher than the uncertainty calculated with eq. 6.1 and 6.2, suggesting that the error bars are underestimated. However, this increase of the relative random error is sill less than 1 % in the sphere-plate separation distance that ranges from 150 to 230 nm, thus not affecting the main results of this manuscript. More exploration and more data are needed to find the explanation for the discrepancy.

6.1.3 Systematic Error Analysis

The main sources of systematic errors are the non-equilibrated motion of the piezoelectric that controls the motion of the sample plate and the non-linear behavior of the piezoelectric. These issues are responsible for modifying the absolute separation distance between the sphere and the plate, leading to a separation distance dependence of the V_0, and making a distance dependence of z_0^*. All of them modify the measured values of the Casmir pressure at certain separation distance.

Systematic error due to the drift of one of the plates: The technique we use for measuring the Casmir pressure requires the separation distance to be constant during the measurement. However, the piezoelectric that controls the sample is not completely in equilibrium when the measurement is performed. Waiting for equilibrium would extend

the data acquisition time from 60 hours to 180 hours or longer, making it impractical. To assure that most of the contribution to the drift of the piezoelectric is negligible during the measurement, every time the separation distance is changed and before starting the measurement, the piezoelectric moving the plate is left to equilibrate for 10 minutes. This procedure reduces the drift to less than 0.3 nm in the following 30 minutes. However, during the experiment, which lasts about 60 hours, we change the separation distance about 50 times in different distance steps. This means, among other thing, that the drift of the piezoelectric plays a larger role at the end of the experiment, when the separation distance is has decreased the most. Its effect seems to be noticeable in the pressure measurements below 145 nm. Using the minimum sphere-plate separation distance dependence z_0^* on the relative sphere-plate separation distance, it has been estimated that the piezoelectric drift for the length of the experiment is about seven nm. The result is a change in values of the Casmir pressure. For example, using the percent uncertainty approach to compare two experimental curves, one that considers the drift and one that does not consider it, the effect of the separation distance drift can be quantified. This comparison shows that at a sphere-plate separation distance of 128 nm, there is -5.9 % percent uncertainty, at 148 nm it is -5.7%, at 166 nm it is -4.9 %, at 177 nm it is 2.1%, and at 384 nm it is -23.5 %. The sign change means that the experimental curves cross and that the curve that does not consider the 7 nm drift is below the one that does consider it. In addition, the value of the percent uncertainty at 384 nm is not important since the error bars of both curves cross each other. The reason it is mentioned, is to show the behavior of both curves, where at distances higher than 300 nm the curves separate

from each other. Note that the contribution of the piezoelectric drift is the least at the separation distance that ranges between 150 nm to 230 nm. This range is where most of the conclusions of this experiment were drawn. To quantify this drift it is needed to measure the motion of the plate throughout the experiment. The device used for this purpose had intermittent noise during the experiment, allowing us to measure the motion of the plate only at the early beginning of the experiment. During the first 10 hours of the T = 6.7 K experiment a drift was not detected. Further inspection of this kind of experiments is needed

A distance dependence of V_0 is generally attributed to the non-equilibrium motion of the piezoelectric that controls the movement of the plate. In the T= 6.7 K experiment this type of dependence was found. In fig. 6.11, the dependence of V_0 with respect to sphere-plate separation distance is shown. At about 210 nm, V_0 starts decreases from a value of -51.7 mV in a linear manner to -60.2 mV at 119.4 nm. The change of V_0 per nanometer is 0.07 mV/nm.

A non-compensated V_0 will produce a residual force on the plate. However, in the analysis, only the residual force in excess of the electrostatic force from the top of the parabola is measured and set equal to the Casimir force. Thus, a change in V_0 is irrelevant as at every point only the residual force is measured. Yet different procedures to analyze the data were devised to reduce the distance dependence of the V_0. One of them will be described below.

To account for this dependence, the time to perform the experiment was effectively reduced by a factor of two. Using measurements at each sphere-plate separation distance that happen earlier in time and ignoring the corresponding

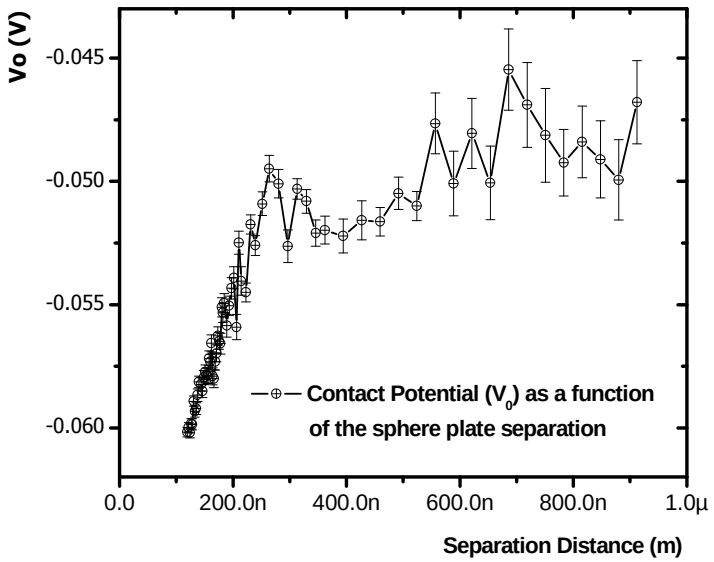

Figure 6.11 Contact potential (V_0) as a function of sphere-plate separation distance at T = 6.7 K

measurements that happen later in time through the data analysis, the results avoids the effects of any separation distance drift which happens for the second half of the measurements. In addition, since the results effectively contain all the information needed to acquire the parameters for obtaining the Casmir pressure, this data analysis method does not affect the overall result. However, this approach was not successful since its results reproduce the distance dependence of fig. 6.11 and the experimental values of fig. 6.1.

Other sources of systematic error have been explored.

Systematic error due to cantilever deflection: The cantilever deflection due to an exerted force on the sphere would lead to the change of sphere-plate separation distance is another possible source of systematic errors. Larger forces then, increase this systematic error more than smaller forces. To account for the deflection, measurement values with lower electrostatic forces were not included on the data analysis. However, the results of this analysis were not substantially different from the case where the bending was not accounted for in the data analysis. Therefore, the conclusion of this analysis was that the effect of the bending of the cantilever on the data is minimal.

To minimize systematic errors on the T= 77 K experiments, the effect of non-constant separation distance due to delayed equilibrium of the piezoelectric was considered. The method to reduce this effect was able to avoid certain features of the distance dependence of the V_0 and z_0^*. The same method that was used for the T = 6.7 K experiments was used here. The sequence in which the voltages V are applied during the electrostatic force measurement can be chosen to be symmetrical around V_0 such that ($V-V_0$) alternately changes from positive to negative starting at its largest positive value. For example, if we applied 10 voltages and the voltage step is ΔV, the first voltage would be $V_0+9\Delta V$, the next one $V_0-8\Delta V$, and the next $V_0+7\Delta V$, and so on till the applied voltage is V_0.

While the deviation of the experimental values at T = 6.7 K with respect to the theoretical curves at short distances has been attributed to systematic errors, the source of the error has not been found yet. As mentioned above, different methods to analyze the data have been tried but none of them seems to affect the results. More exploration and

more T = 6.7 K data is needed to understand the systematic errors in the experimental setup of this manuscript at this temperature.

6.2 Casimir force between two Au plates at T = 77 K

The measurements at this temperature were not as successful as the measurements at T = 6.7 K. Their precision was significantly lower and the contact potential V_0 is above 100 mV. The latter suggests that the sphere or sample is in some way contaminated. This is because the residual potential V_0 between two gold plates should be in principle be negligible. Furthermore, for the same sphere plate set V_0 had three different values for three different temperatures. At T = 300 K it was ~ 70 mV, at T = 77 K, 430 mV, and at T = 6.7 K, it decreased to ~ 50 mV. Even when the thermal expansion from liquid Nitrogen temperatures to the base temperature of the AFM is small, the change of V_0 by an order of magnitude could imply a change in the area of region between the sphere and the plate. However, the change of V_0 with separation distance was almost identical for both temperatures, suggesting that the area of closest approach remained the same or that a similar drift was occurring at two different temperatures. The latter was not further pursued because any systematic errors should be noticeably different in these two temperatures. In addition, since the method of analysis has been thoroughly tested, the authors of this manuscript believe that it will not introduce such a behavior of V_0. More exploration is needed. The Casmir pressure measured in the case where V_0 ~ 420 mV is shown in fig. 6.12. The experimental values are compared to the theoretical values of the pressure at T = 77 K calculated with the generalized Drude-like model.

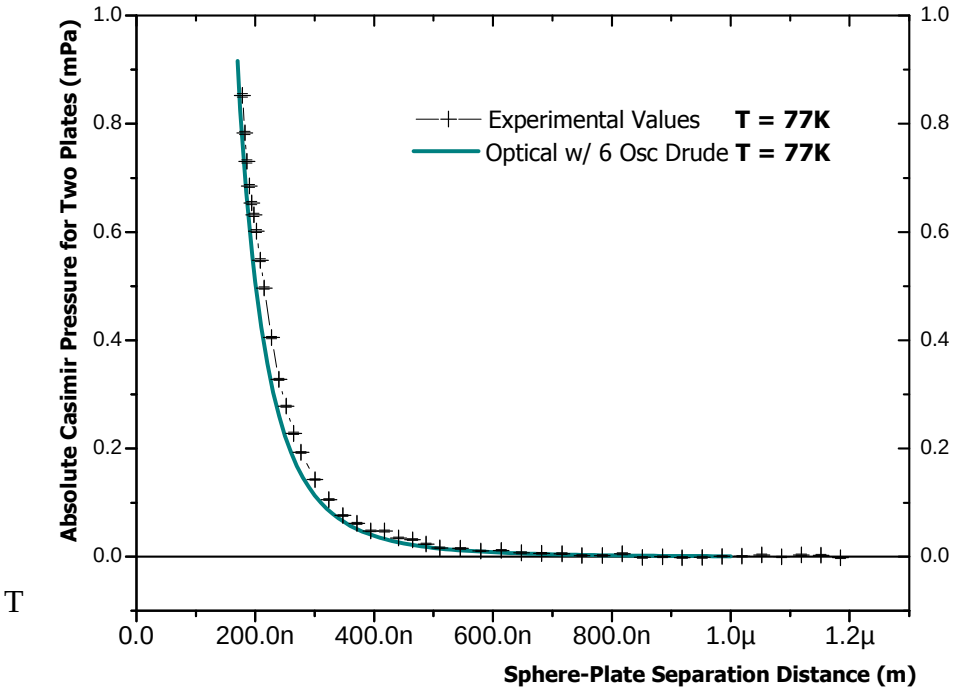

T

Figure 6.12. Experimental and theoretical values for the absolute Casmir pressure between two plates as a function of the sphere-plate separation distance for T = 77 K. The dark cyan solid line is the Casmir pressure between two plates calculated using the generalized Drude-like model at T = 77 K. The black crosses are the experimental values measured at T = 77 K with their corresponding error bars.

he results in fig. 6.12 do not match the theoretical curve and the experimental curve does not have the same curvature as the latter. This indicates that systematic errors are present. Careful analysis of the data in the manner of the T= 6.7 K data was done and it does not produce satisfactory results. In fig 6.12 the experimental data obtained at T = 77 K is shown. The data was analyzed with the same method that was used for the T= 6.7 K experiment.

While most of the instrument standards, calibrations and measurements were taken at T = 77 K, there was never data as good as the data taken at T = 6.7 K. This

suggests that at T = 77 K a drift in the separation distance might be present, considerably altering the experimental pressure curves. An argument against the latter is that if the total drift is estimated with measured values of the motion of the plate, it can be used to reduce the effects of this systematic error. The experimental curves are nevertheless not modified when this is performed. This indicates that another source of a systematic error must be the dominant source. It has been suggested that a possible candidate for this error is an electrostatic effect of the cantilever fiber end on the modified cantilever. This effect is more prominent for shorter distances between the fiber end and the cantilever. While this separation is ~ 50 to 100 μm at T = 300 K, the final separation at T= 77 K might be different. This effect has nevertheless not shown any measurable contribution at the separation distance where the Casmir pressure has been measured in this experimental study. More exploration is needed at larger sphere-plate separation distances > 2 μm, where the fiber-cantilever interaction, not the sphere-plate interaction, is most dominant.

The experiments performed at this temperature suggest that another method, one that minimizes the effect of the sphere plate separation distance drift, by a rapid collection of data, would be a better option at this temperature. FM-AFM is a very good candidate for the rapid measurement.

6.3 Casimir pressure between two Au plates at T = 300 K

The experiments measured at this temperature showed the largest deviations with respect to the theoretical curves. Mechanical drift is most likely to be the dominant contribution of the deviation since the interferometer that measures the relative motion of the plate can detect large changes. Even when the drift is measured with an independent detector, the measurement procedure used did not allow an effective subtraction of the drift. An example of the experimental curves obtained at T = 300 K is in fig. 6.13.

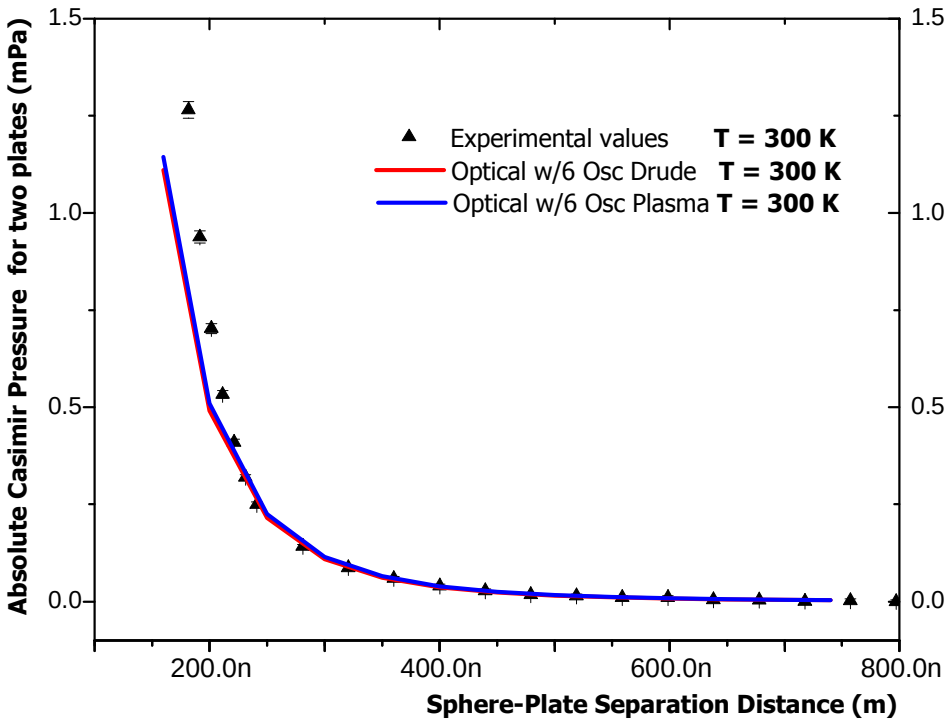

Figure 6.13 Experimental and theoretical values for the absolute Casmir pressure between two plates as a function of the sphere-plate separation distance for T = 300 K. The triangles are the experimental values measured at T = 77 K. The error bars are the size of the symbols or less. The red solid line is the Casmir pressure between two plates calculated using the generalized Drude-like model at T = 300 K. The dark blue solid line is the Casmir pressure between two plates calculated using the generalized Plasma-like model at T = 300 K.

In summary, the results at T = 6.7 K could be used to determine the thermal effects of the Casimir force. The reason is that they have a high degree precision due to the lower systematic errors resulting from the drift of the sphere-plate separation. In contrast, higher temperatures results do not have the expected precision. While in these cases, the mechanical drifts should be more significant than in the low temperature case, the procedure to subtract their contribution is not possible given the measurement method used. It is important however, that the motion of the plate is measured accurately throughout the separation distance where the measurements are performed. Another possibility is to use different methods of cantilever response to measure the Casimir pressure. A method that reduces the effects of mechanical drifts is the FM-AFM technique. In the FM-AFM technique, the data taking time is reduced by a factor of 20 and thus the effects of drifts will be correspondingly reduced. The instrument used in this experimental study is being modified to implement this technique in future experiments.

7 Conclusions and Future Prospects

We have measured the Casmir pressure between two Au plates at T = 6.7 K, T = 77 K, and at T=300 K at a sphere-plate separation distance of 120 nm to 600 nm. This has been achieved through use of a variable temperature atomic force microscope that we built to detect the thermal effects of the Casmir force. In the sphere-plate separation distance from 145 nm to 230 nm, the degree of agreement between the results from the measurements at T = 6.7 K and the theoretical values of the Casmir pressure calculated with the generalized Drude-like model at T = 6.5 K is 2%. Furthermore, their relative random error at this separation distance is less than 1 %. In contrast, the degree of agreement of these same values and the theoretical values of the Casmir pressure at T = 300 K using the Drude-like model pressure is about 4%. The large discrepancies in the degrees of agreement could be used to measure the thermal effects of the Casmir pressure predicted by the generalized Drude-like model. The outcome of these measurements would reveal the role played by the dissipation of the constituent material of the plates in the context of the Casmir effect at non-zero temperatures for real materials. In addition, measuring the thermal effects of the Casmir force would solve long-standing disputes about the model that better describes the material of the plates using the Lifshitz's approach.

In contrast to the results at T= 6.7 K, our measurements of the Casmir pressure at T = 300 K and at T = 77 K had a more limited outcome. They were significantly affected by systematic errors, which reduced their expected precision. Mostly, these errors were attributed to the mechanical drift associated with the specific motion of the plate in our

measuring technique during the duration of the measurement. Approaches to subtract this drift were not successful in our measurement methodology. Different experimental stabilization schemes such as using feedback controls on the actuator did not achieve the necessary precision. We have concluded that it is more effective to avoid the drift altogether by using a detection method that substantially reduces the duration of the experiment. A technique called frequency modulation atomic force microscopy is able to perform such a measurement. In addition, it has already proven to be a high sensitivity tool to explore the Casmir effect in our lab. This technique can not only reduce the systematic errors but it can also enhance the resolution of our instrument by an order of magnitude at T = 6.7 K. Furthermore, the modifications required for our instrument to employ this measuring technique are straightforward. These are the reasons why our future measurements will be performed with this technique. If successful, measurements of the Casmir pressure between two plates at three different temperatures could be directly compared and the thermal effects of the Casimir effect measured.

This sensitive technique and the capability to change the temperature of the sphere-plate system will make our instrument a powerful tool to explore new phenomena in the Casmir field. Such is the case of the Casmir effect on materials that undergo a phase transition with temperature. For example, it has been suggested that the study of Mott insulators [105] -materials that experience an abrupt change from high electrical resistivity to low resistivity- could help understand the role of free charge carriers in the Lifshitz's approach [105]. Another example is of superconductor materials, which have zero resistivity below a critical temperature. Bimonte [106] has suggested that the

thermal effects of the Casmir effect can be explored in a sphere-plate superconductor cavity made of Niobium (Nb) or Au and Nb Since phase transition of this material occurs at T = 9.3 K, its critical temperature falls in the temperature range of our instrument, making Casmir force experiments with superconductor materials simple to setup. In addition, during the superconductor transition, the change of the Casmir energy can be comparable to the condensation energy of a semiconducting film. This means that an increase in the value of the critical magnetic field can be measured [107]. Another example worth mentioning is in the study of the Casmir force dependence on non-trivial geometries. Recently, Maghrebi et al. [108] have calculated a large temperature dependence of the force between a conductive cone and a plate. This effect is observed for cones with similar dimensions to the tips of commercially available cantilevers. In summary, these examples point out that in addition to the results obtained; the instrument built for and described in this thesis has exceptional advantages that will be exploited to rapidly push the frontier of the field of Casimir effect in the near future. .

8 Appendix A Pictures of the Laboratory

In this appendix the pictures of the main components of the instrument are presented.

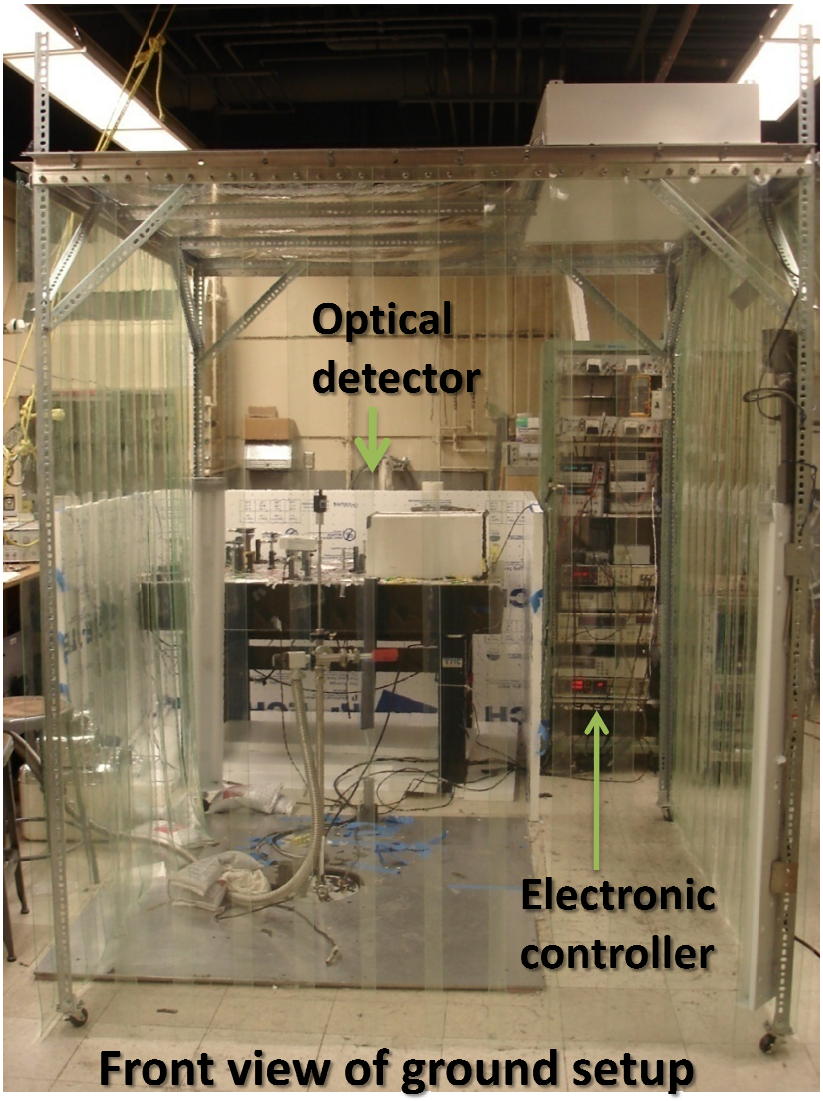

This is the view of the floor components of the instrument. In the background is the optical table with the two all-fiber interferometers and its components. Two optical fiber strands run from the interferometer to the cryostat. The latter is in a cement pit under the floor level. The pit is covered with the aluminum plates. The area where the sample and

sphere are manipulated is particle-free due to the home-built clean room.

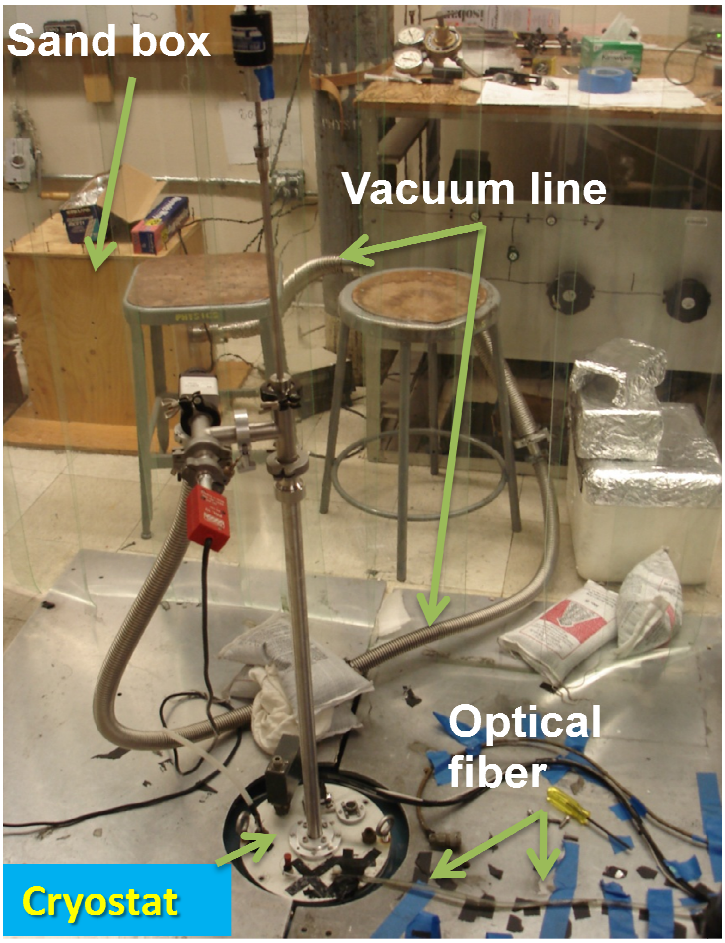

This picture shows the cryostat from the top. It includes the main vacuum line, the vibration isolation system, the optical fibers, and the linear manipulator.

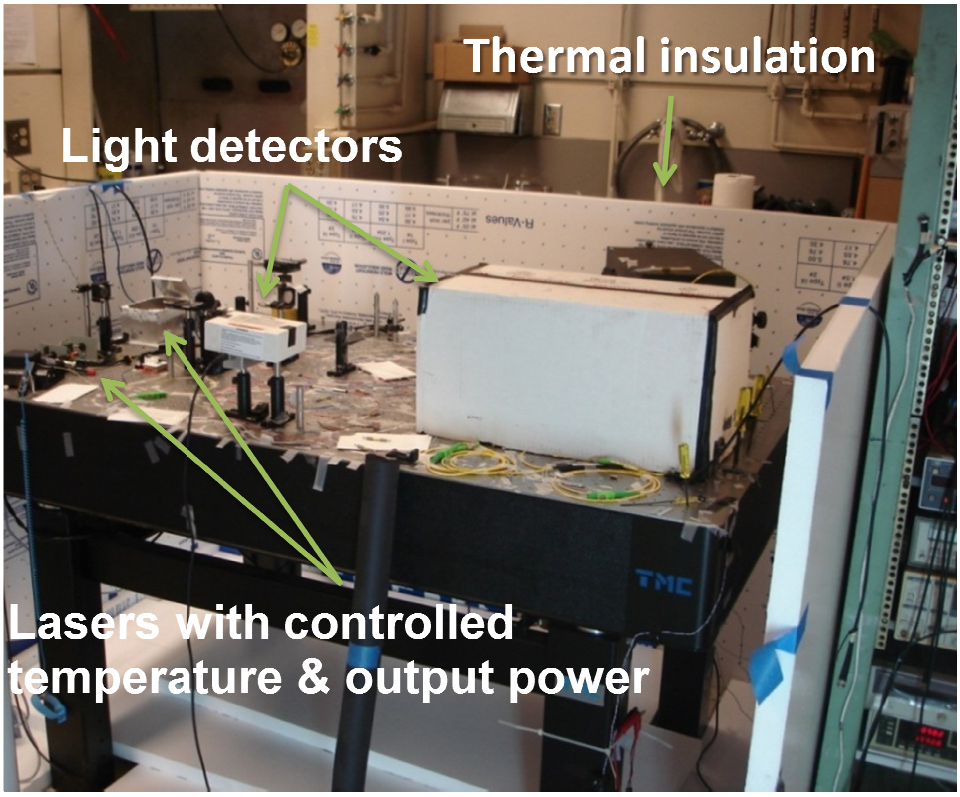

This picture shows a close up of the optical table and its components.

9 References

[1] U. Mohideen, and A. Roy, Physical Review Letters **83**, 3341 (1999).
[2] R. S. Decca *et al.*, Phys. Rev. Lett. **91**, 050402 (2003).
[3] H. B. Chan *et al.*, Phys. Rev. Lett. **87**, 211801 (2001).
[4] M. Kardar, and R. Golestanian, Reviews of Modern Physics **71**, 1233 (1999).
[5] M. E. Fisher, and P. G. d. Gennes, C. R. Seances Acad. Sci. **287**, 207 (1978).
[6] M. C. R. Garcia, Physical Review Letters **83**, 1187 (1999).
[7] P. W. Milonni, *The Quantum Vacuum: An introduction to Quantum Electrodynamics* (Academic Press, N.Y. , 1994).
[8] S. Weinberg, Rev. Mod. Phys. **61**, 1 (1989).
[9] R. L. Jaffe, Physical Review D **72**, 021301 (2005).
[10] M. Bordag, U. Mohideen, and V. M. Mostepanenko, Physics Reports-Review Section of Physics Letters **353**, 1 (2001).
[11] H. B. G. Casimir, Proc. Kon. Ned. Akad. Wet. **51**, 793 (1948).
[12] E. M. Lifshitz, Sov. Phys. JETP, **2** (1956).
[13] M. Bordag *et al.*, *Advances in the Casimir Effect* (Oxford Univesity Press, Oxford, 2009), p. 760 pages.
[14] J. Schwinger, L. L. D. Jr., and K. A. Milton, Ann. Phys. (N.Y.) **115**, 1 (1978).
[15] F. M. Serry, D. Walliser, and G. J. Maclay, Journal of Applied Physics **84**, 2501 (1998).
[16] M. Elwenspoek, and R. Wiegerink, *Mechanical Microsensors* (Springer-Verlag, 2001).
[17] M. J. Sparnaay, Physica **24**, 751 (1958).
[18] J. N. Israelachvili, and D. Tabor, Proc. Roy. Soc. Lond. A **331**, 19 (1972).
[19] D. Tabor, and R. H. S. Winterton, Nature **219**, 1120 (1968).
[20] P. H. G. M. v. Blokland, and J. T. G. Overbeek, J. Chem. Soc. Faraday Trans. **74**, 2637 (1978).
[21] U. Mohideen, and A. Roy, Phys. Rev. Lett. **81**, 4549 (1998).
[22] F. Chen *et al.*, Phys. Rev. Lett. **88**, 101801 (2002).
[23] F. Chen *et al.*, Physical Review B **76**, 15 (2007).
[24] H. B. Chan *et al.*, Science **291**, 1941 (2001).
[25] S. K. Lamoreaux, Physical Review Letters **78**, p. 5 (1997).
[26] S. K. Lamoreaux, Phys. Rev. Lett. **78** (1998).
[27] F. Chen *et al.*, Physical Review Letters **97**, 4 (2006).
[28] U. Mohideen, and A. Roy, Physical Review Letters **81**, 4549 (1998).
[29] S. K. Lamoreaux, Rep. Prog. Phys. **68**, 201 (2005).
[30] K. A. Milton, *The Casimir effect* (World Scientific, Singapore, 2001).
[31] M. Bostrom, and B. E. Sernelius, Phys. Rev. Lett. **84**, 4757 (2000).
[32] K. A. Milton, J. Phys. A: Math. Gen. **37**, R209 (2004).
[33] I. Brevik *et al.*, J. Phys. A: Math. Theor. **41**, 164017 (2008).
[34] M. Bostrom, and B. E. Sernelius, Physica A **339**, 53 (2004).
[35] J. S. Hoye *et al.*, Phys. Rev. E **75**, 051127 (2007).

[36] R. S. Decca *et al.*, Physical Review D **75**, 077101 (2007).
[37] I. Brevik, and K. A. Milton, Physical Review E **78**, 011124 (2008).
[38] B. E. Sernelius, Physical Review A **80**, 043828 (2009).
[39] G. Jourdan *et al.*, EPL **85**, 31001 (2009).
[40] B. Derjaguin, Kolloid-Z **69**, 155 (1934).
[41] T. Emig, in *JOURNAL OF STATISTICAL MECHANICS-THEORY AND EXPERIMENT* (IOP PUBLISHING LTD, DIRAC HOUSE, TEMPLE BACK, BRISTOL BS1 6BE, ENGLAND, 2008), p. P04007.
[42] P. A. M. Neto, A. Lambrecht, and S. Reynaud, Phys. Rev. A. **78**, 012115 (2008).
[43] M. Bordag, U. Mohideen, and V. M. Mostepanenko, Phys. Rep. **353**, 1 (2001).
[44] D. E. Krause *et al.*, Physical Review Letters **98**, 050403 (2007).
[45] A. Canaguier-Durand *et al.*, Phys. Rev. Lett. **104**, 040403 (2010).
[46] R. Zandi, T. Emig, and U. Mohideen, Phys. Rev. B. **81**, 195423 (2010).
[47] P. W. Milonni, and M.-L. Shih, Phys. Rev. A **45**, 4241 (1992).
[48] N. G. V. Kampen, B. R. A. Nijboer, and K. Schram, Phys. Lett. **26A**, 307 (1968).
[49] G. L. Klimchitskaya *et al.*, Physical Review A **60**, 3487 (1999).
[50] F. Chen *et al.*, Physical Review A **69**, 022117 (2004).
[51] V. B. Bezerra, G. L. Klimchitskaya, and C. Romero, Int. J. Mod. Phys. A **16**, 3103 (2001).
[52] A. Lambrecht, M.-T. Jaekel, and S. Reynaud, Physics Letters A **225**, 188 (1997).
[53] T. Emig *et al.*, Phys. Rev. A **67** (2003).
[54] A. Lambrecht, and V. N. Marachevsky, Physical Review Letters **101**, 160403 (2008).
[55] A. Roy, and U. Mohideen, Phys. Rev. Lett. **82**, 4380 (1999).
[56] H. C. Chiu *et al.*, Physical Review B (Rapid Communication) (2009).
[57] G. L. Klimchitskaya, U. Mohideen, and V. M. Mostepanenko, Reviews of Modern Physics **81**, 1827 (2009).
[58] P. C. Martin, and J. Schwinger, Physical Review **115**, 1342 (1959).
[59] M. Bordag *et al.*, Phys. Rev. Lett. **85**, 503 (2000).
[60] L. S. Brown, and G. J. Maclay, Physical Review **184**, 1272 (1969).
[61] J. Mehra, Physica **37**, 145 (1967).
[62] G. L. Klimchitskaya, U. Mohideen, and V. M. Mostepanenko, Journal of Physics A-Mathematical and General **40**, F339 (2007).
[63] E. D. Palik, *Handbook of Optical Constants of Solids* (Academic Press, N.Y. , 1985).
[64] I. Brevik *et al.*, PHYSICAL REVIEW E **71** (2005).
[65] J. S. Hoye *et al.*, Physical Review E **67**, 056116 (2003).
[66] G. L. Klimchitskaya, and V. M. Mostepanenko, Phys. Rev. A **63**, 062108 (2001).
[67] R. S. Decca *et al.*, European Physical Journal C **51**, 963 (2007).
[68] V. B. Bezerra, G. L. Klimchitskaya, and V. M. Mostepanenko, Physical Review A **66**, 062112 (2002).
[69] H. J. Mamin *et al.*, Nat Nano **2**, 301 (2007).
[70] D. M. Eigler, and E. K. Schweizer, Nature **344**, 524 (1990).
[71] F. J. Giessibl, Reviews of Modern Physics **75**, 949 (2003).

[72] G. Binnig *et al.*, Physical Review Letters **49**, 57 (1982).
[73] R. Wiesendanger, *Scanning Probe Microscopy and Spectroscopy: Methods and Applications* (Cambridge University Press, 1994).
[74] C. J. Chen, *Introduction to scanning tunneling microscopy* (Oxford University Press, 1993).
[75] J. Loos, Adv. Mater. **17**, 1821 (2005).
[76] D. Rugar *et al.*, Applied Physics a-Materials Science & Processing **72**, S3 (2001).
[77] F. Chen *et al.*, Physical Review A **66**, 032113 (2002).
[78] A. Roy, C. Y. Lin, and U. Mohideen, Physical Review D **60**, (R)111101 (1999).
[79] J. N. Munday, F. Capasso, and V. A. Parsegian, Nature **457**, 170 (2009).
[80] H. B. Chan *et al.*, Physical Review Letters **87**, 211801 (2001).
[81] H. J. Mamin, and D. Rugar, Applied Physics Letters **79**, 3358 (2001).
[82] S. de Man, K. Heeck, and D. Iannuzzi, Physical Review A **79**, 024102 (2009).
[83] S. de Man *et al.*, Physical Review Letters **103**, 040402 (2009).
[84] S. de Man, K. Heeck, and D. Iannuzzi, Physical Review A **82**, 062512 (2010).
[85] G. Binnig, C. F. Quate, and C. Gerber, Physical Review Letters **56**, 930 (1986).
[86] G. Binnig, and H. Rohrer, Reviews of Modern Physics **71**, S324 (1999).
[87] F. Ohnesorge, and G. Binnig, Science **260**, 1451 (1993).
[88] T. R. Albrecht *et al.*, Journal of Applied Physics **69**, 668 (1991).
[89] F. J. Giessibl, Science **267**, 68 (1995).
[90] SRS, Stanford Research Systems **100 kHz FFT Spectrum Analyzer SR770**.
[91] F. Reif, *Fundamentals of Statistical and Thermal Physics* (McGraw-Hill Science, 1965).
[92] H. C. Chiu *et al.*, Journal of Physics A-Mathematical and Theoretical **41**, 1 (2008).
[93] G. Torricelli *et al.*, Physical Review A **82**, 010101 (2010).
[94] H. B. Chan *et al.*, Physical Review Letters **101**, 030401 (2008).
[95] R. S. Decca *et al.*, PHYSICAL REVIEW D **68** (2003).
[96] R. C. Richardson, and E. N. Smith, *Experimental Techniques In Condensed Matter Physics At Low Temperatures* (Westview Press 1998).
[97] B. C. Stipe, M. A. Rezaei, and W. Ho, Review of Scientific Instruments **70**, 137 (1999).
[98] D. Vespel, and http://www2.dupont.com/Vespel/en_US/.
[99] MikroMasch, C. t. n. Al, and www.spmtips.com.
[100] 3M, Scothlite Glass Bubbles (P/N A16/500).
[101] Edmunds Scientific (P/N NT68-157).
[102] S.-i. Park, and C. F. Quate, Review of Scientific Instruments **58**, 2004 (1987).
[103] M. Roseman, and P. Grutter, Review of Scientific Instruments **71**, 3782 (2000).
[104] R. Castillo-Garza *et al.*, Journal of Physics: Conference Series **161**, 012005 (9 pp.) (2009).
[105] R. Castillo-Garza *et al.*, Physical Review A **75**, 062114 (2007).
[106] G. Bimonte, Physical Review A **78**, 062101 (2008).
[107] G. Bimonte *et al.*, Phys. Rev. Lett. **94**, 180402 (2005).
[108] M. F. Maghrebi *et al.*, arXiv:1010.3223v1 (2010).